aerospace

MDPI

Article

Thermal Design and Analysis of the CubeSat ERMIS-3

Konstantinos-Panagiotis Bouzoukis [1,*], Vaios Lappas [2] and Vassilis Kostopoulos [1]

[1] Applied Mechanics Laboratory, Department of Mechanical Engineering and Aeronautics, University of Patras, Patras University Campus, GR26504 Rion, Achaia, Greece; kostopoulos@upatras.gr
[2] Department of Aerospace Science and Technology, National and Kapodistrian University of Athens, Evripos Campus, GR34400 Psachna, Evia, Greece; valappas@aerospace.uoa.gr
* Correspondence: kbouzoukis@ac.upatras.gr

Abstract

This work presents the thermal design and analysis of ERMIS-3, one of the three satellites of the ERMIS Hellenic CubeSat Demonstration Mission. All the primary external heat sources were considered in this study, along with the heat dissipated by the sub-systems of the satellite during its various modes of operation. During the analysis, several heat sources, such as subsystem and payload operation or battery pack heating elements, are activated and deactivated by implicit and explicit events instead of only using orbit-averaged heat dissipation values to improve the thermal model's accuracy. Moreover, in parallel with the thermal analysis, a calculation of the solar radiation that is incident to the solar cells of the satellite takes place, providing the model with a good approximation of the amount of solar radiation that is converted into electrical power. The calculation of the generated electrical power is used to realistically model the heat dissipation of the electrical power system. In terms of results, four different thermal cases are presented, which practically cover the extreme hot and cold scenarios that the CubeSat ERMIS-3 could face during its orbital operations. Finally, the temperatures predicted by the thermal model are correlated with in-orbit temperature measurements acquired through telemetry.

Keywords: satellite; CubeSat; satellite thermal design; satellite thermal analysis; satellite thermal control; finite element method

1. Introduction

CubeSats are small satellite platforms that follow a standardized structural architecture and make extensive use of COTS components, rendering them affordable to design, manufacture, integrate, test and launch in comparison to larger, not-standardized platforms. This has enabled countries and institutions with limited financial and technological resources such as universities and start-ups, with otherwise limited access to space, to engage in a wide range of orbital operations. The types of missions undertaken by CubeSat platforms commonly include Earth observation and science, telecommunications, asset monitoring, astronomy, deep-space exploration, chemical and biological experimentation, and novel technology demonstration. Moreover, CubeSats may operate as individual platforms or as distributed nodes of larger constellations [1,2].

In a manner similar to their larger counterparts, CubeSats are expected to survive and operate successfully in the hostile thermal environment of space. Therefore, the need for a thorough thermal design and thermal analysis is of significant importance for CubeSats as well. Moreover, it should be noted that the small size of CubeSats leads to close packaging of heat-dissipating electronic components while also constraining the design team in terms

Check for updates

Academic Editor: Xiao-Wei Gao

Received: 1 October 2026
Revised: 17 November 2026
Accepted: 19 November 2026
Published: 21 November 2026

Copyright: © 2026 by the authors. Licensee MDPI, Basel, Switzerland. This article is an open access article distributed under the terms and conditions of the Creative Commons Attribution (CC BY) license.

of thermal design and control options, as the volume that is available to CubeSat designers renders the implementation of active thermal control systems problematic in the majority of cases. For this reason, the design of an effective passive thermal control system is of paramount importance in the case of CubeSats and other small satellites. The first step in ensuring that the thermal design of a CubeSat is correct and no subsystems of the satellite will violate their maximum and minimum allowable temperature limits when in orbit is the performance of an analysis that simulates the orbital thermal behavior of the satellite for all its principal operational modes, in conjunction with the expected extreme environmental conditions the satellite is going to face when in orbit. Due to their complexity, thermal analyses of satellites are typically performed through the use of dedicated Finite Element (FE) software packages. Examples of such software packages include the ESATAN-TMS (ITP Engines UK Ltd., Hucknall, England, UK) [3], the Ansys Thermal Desktop (Ansys, Inc., Canonsburg, PA, USA) [4], COMSOL Multiphysics® Heat Transfer Module (COMSOL AB, Stockholm, Sweden) [5], and Radian (Radian Space, S.L., Madrid, Spain), which is a cloud-based thermal analysis software [6].

Based on the results of a satellite thermal analysis, various passive or active thermal control techniques and systems can then be implemented to control, optimize or alter the thermal behavior of the satellite and by extension, manage the temperatures of its individual subsystems. Examples of passive thermal control solutions include surface coatings, Multi-Layer Insulation blankets, radiators, passive louvers, thermal straps, heat pipes, and thermal storage units containing Phase-Change Materials. Active thermal control solutions include systems such as electrical heating elements, pumped fluid loops, active louvers, cryocoolers, and thermoelectric coolers. More information about such thermal control solutions for small satellite platforms can be found in the National Aeronautics and Space Administration's (NASA) Small Spacecraft Technology State-of-the-art report [7].

Over the years, the field of thermal design and analysis of CubeSats has attracted the interest of researchers around the world, with a notable example of a detailed CubeSat thermal analysis being the work of Garzón et al. in [8], where the effect of beta (β) angle (the angle formed between the satellite's orbital plane and the solar vector) is investigated, along with an analysis regarding the effect of the thermal contact conductance values that are utilized in the thermal model of a 3U CubeSat. Another example of detailed CubeSat thermal design and analysis work is that of Chandrashekar [9], which presents the thermal design and analysis of the 3U CubeSat MIST. In this instance, the thermal analysis showed that certain mission-critical systems of the satellite could violate their required operational temperature limits during some orbital thermal condition scenarios, highlighting the need for a thermal design revision. One more notable CubeSat thermal analysis work is that of Blanchete and Bah in [10], where plastic and elastic theoretical models for the calculation of thermal contact conductance values were used in a 3U CubeSat thermal model that was created in COMSOL Multiphysics. The results provided by the thermal model were correlated with a thermal balance test and it was found that the Cooper–Mikic–Yovanovich plastic model is the one that is best suited for CubeSat applications. Moreover, as exhibited by Cisneros Ortega et al. in [11], a CubeSat thermal analysis can also be coupled with a detailed FE structural model that can be used to predict the level of thermal stresses that the temperature changes of the orbital environment are going to be translated into during the in-orbit operation of a CubeSat. Finally, certain institutions have worked on guidelines about the thermal modeling and analysis of CubeSats, with a notable example being the guide published with support from the United States Air Force Research Laboratory under the title; Small Satellite Thermal Modeling Guide [12].

The present work focuses on the thermal design and analysis of the CubeSat ERMIS-3, mainly focusing on demonstrating the procedure that was followed for the thermal mod-

eling of the satellite and the obtained results that serve as an indication of its ability to withstand the thermal environment it is set to face during its mission. It is thus structured in the following manner. First, Section 2 presents an overview of the design and the subsystems of ERMIS-3, along with the design choices that stem from the thermal characteristics of certain subsystems. Section 3 provides some key information on the Low Earth Orbit (LEO) thermal environment. The procedure that was followed for the creation of the thermal FE model of ERMIS-3 is then covered in detail in Section 4. Section 5 begins with the definition of the thermal environment considered for the different cases of the analysis and presents the results of the radiation analysis simulations through which the solar band and ambient band radiative fluxes that are incident to the external surfaces of the satellite in the examined thermal cases are calculated. The detailed results of the thermal analysis of ERMIS-3 are presented in Section 6, with the calculated temperatures being compared to the allowable temperature limits for each of the satellite's subsystems. Section 7 then presents a comparison between the predicted temperature ranges determined by the FE thermal model of ERMIS-3 and in-orbit temperature measurements, for a series of major platform components of the satellite. Finally, Section 8 presents the primary conclusions that stem from the thermal modeling and analysis of ERMIS-3.

2. The CubeSat ERMIS-3, Its Mission, and Aspects of Its Thermal Design

ERMIS-3 is an advanced 8U CubeSat that is part of the ERMIS Hellenic CubeSat Demonstration Mission. The ERMIS mission consists of three CubeSats placed in a Sun-Synchronous Orbit (SSO) that share a common bus. ERMIS-1&2 are 6U CubeSats and have the objective of demonstrating LEO Non-Terrestrial 5G-Internet of Things telecommunications and inter-satellite communications. ERMIS-3 on the other hand aims to demonstrate hyperspectral Earth observation through image acquisition over the Hellenic territory, in-orbit lossless and near lossless image compression, and laser-optical telecommunication technologies for the downlink of data to the optical ground station of the mission. The data acquired by the hyperspectral imager of the satellite ERMIS-3 can be utilized for applications that include ground fertility mapping and precision agriculture, water quality monitoring, and natural disaster evaluation, among other types of applications. The three satellites of the ERMIS mission were developed by a consortium consisting of the National and Kapodistrian University of Athens (NKUA), OQ Technology Hellas (Athens, Greece), the University of Patras, the University of the Aegean, and the National Observatory of Athens. The entire project was overseen by the European Space Agency (ESA) on behalf of the Greek Ministry of Digital Governance.

To perform its mission, the CubeSat ERMIS-3 is equipped with the ATLAS laser-optical communications terminal which is developed by Astrolight (Vilnius, Lithuania) and consists of a Free-Space Optics (FSO) assembly and a fiber amplifier assembly. The ATLAS laser-optical communications terminal can achieve data transmission rates that exceed 1 Gbps, utilizing a 1553.3 nm wavelength laser-beam for transmission [13]. The satellite is also equipped with the Simera Sense (Leuven, Belgium) HyperScape100 hyperspectral imager, which is capable of acquiring images across part of the visible and near-infrared portion of the electromagnetic spectrum with a Ground Sampling Distance of 4.75 m and a swath of 19.40 km from an altitude of 500 km [14]. Its operation is supported by a COTS Payload Data Processing Unit (PDPU) and a satellite bus developed by GomSpace (Aalborg, Denmark) [15], coupled with the CubeSpace (Stellenbosch, South Africa) Generation-2 Turn-Key Attitude Determination and Control System (ADCS) [16] and the PST3S-H2 star tracker, which was manufactured by TY-Space Technology Ltd. (Beijing, China) [17].

An overview of ERMIS-3 in its deployed configuration is presented in Figure 1, along with annotations that highlight some of its externally mounted components. In a similar

manner, Figure 2 presents the internal configuration of ERMIS-3 with the mission-enabling payloads as well as the subsystems that make up the satellite's bus being annotated. These figures also depict the satellite's reference system, which is located at the geometric center of the 8U structural frame. All the aforementioned figures depict the satellite's detailed Computer Aided Design (CAD) model, which was created using the Autodesk Inventor Professional 2023 CAD software (Autodesk, Inc., San Francisco, CA, USA) [18].

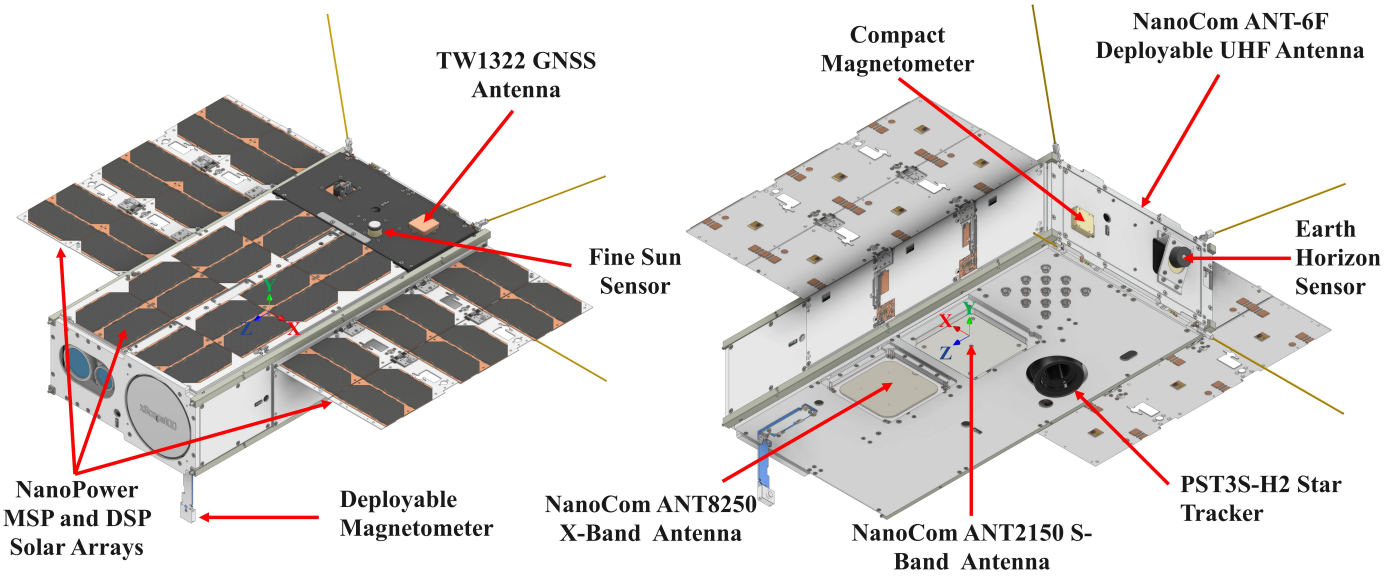

Figure 1. CAD renderings showing the exterior of ERMIS-3 in its deployed configuration.

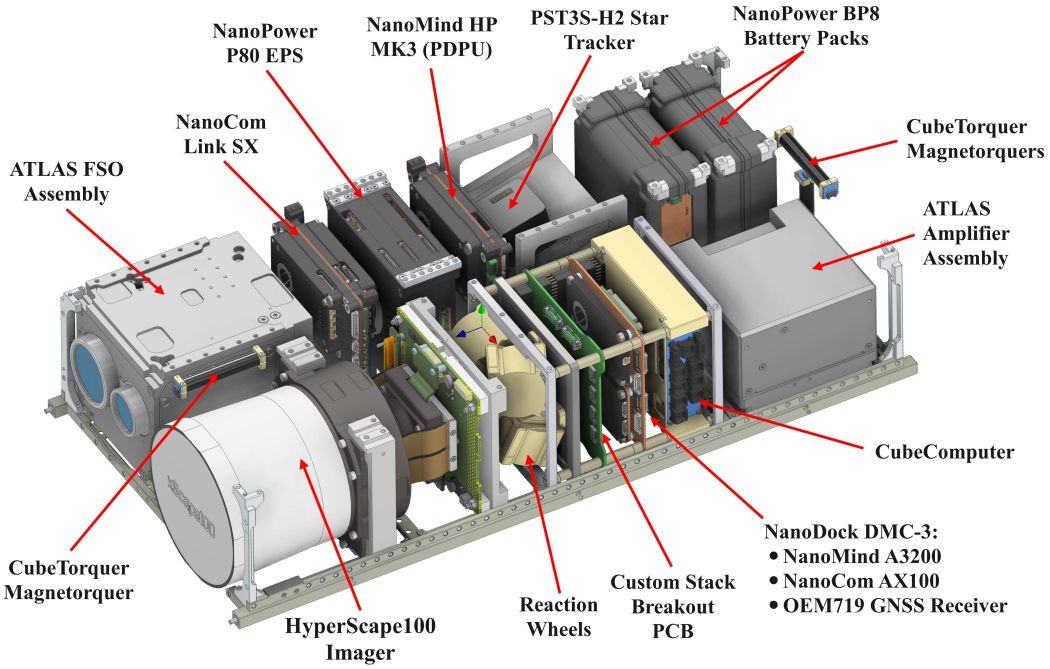

Figure 2. A CAD rendering of ERMIS-3 that presents the internally mounted payloads and platform subsystems of the CubeSat.

All the aluminum panels that cover the exterior of ERMIS-3, either COTS or custom-made ones, have undergone appropriate surface treatments. More specifically, some components have been subjected to sulfuric acid anodization [19] in the form of either non-dyed (clear) anodization (MIL-A-8625 Rev. F Type II Class 1) or black-dyed anodization (MIL-A-8625 Rev. F Type II Class 2), while some COTS components of the satellite have been subjected to chromium(VI)-free passivation according to the MIL-DTL-5541 Rev. F Type II

Class 3 standard using SurTec® 650 [20]. The different anodization treatments performed on the external panels serve to both protect the aluminum from atomic oxygen corrosion [21], as well as to create an appropriate exterior surface for ERMIS-3 that exhibits a delicate balance between absorptivity against the short-wavelength solar radiation and emissivity in the infrared (IR) region of the electromagnetic spectrum. In this way, the amount of thermal energy that is absorbed and rejected by the satellite is optimized so that the satellite may be able to maintain its individual subsystems and payloads in an optimal temperature range during all of its different modes of operation and for any of the potential fluctuations of the orbital thermal conditions. In that regard, some of the most significant surface treatments applied on the external surfaces of ERMIS-3 (both COTS and custom-made) are visualized in Figure 3.

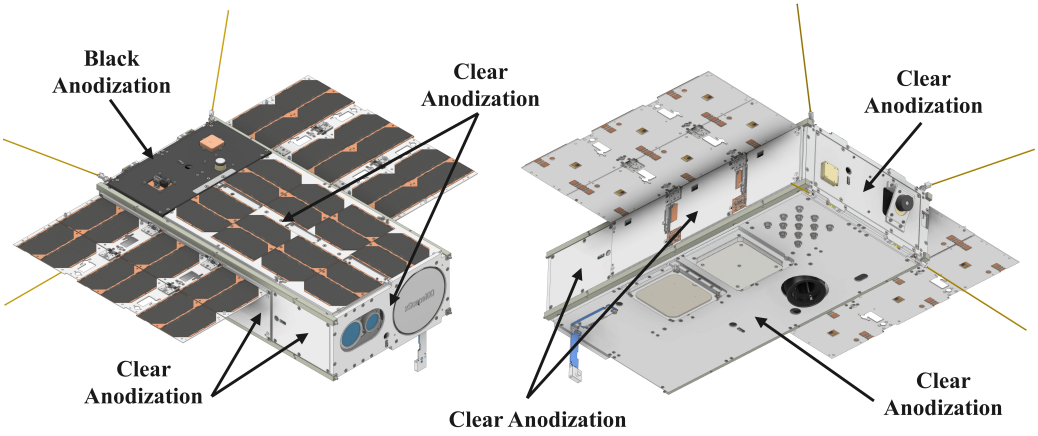

Figure 3. CAD renderings of ERMIS-3 showing surface treatments applied on the CubeSat's exterior.

The fiber amplifier assembly of the ATLAS laser-optical communications terminal is very important to the thermal design of ERMIS-3, as when operational, its heat dissipation is significant. For this reason, the ATLAS amplifier assembly is specifically designed to be mounted directly on a flat, rigid surface through the use of 13 M4 threaded holes. These M4 holes were utilized to couple the amplifier directly to the -Y external aluminum panel of the satellite. In this way, the heat dissipated by the amplifier is transferred directly to the -Y aluminum cover panel, which in turn acts as a radiator due to the high IR emissivity of clear anodization, rejecting the module's heat to space and ensuring it would not overheat during operation. The high fastening torque applied on the M4 screws along with their large quantity ensures that an excellent thermal contact between the amplifier and the aluminum panel parts is established. Moreover, during the manufacturing of the -Y aluminum panel a surface roughness of Ra 0.8 μm was designated, which also facilitates the establishment of an appropriately high thermal contact between the amplifier assembly and the aluminum panel. Furthermore, the ATLAS amplifier module used for the ERMIS mission was also specifically modified by Astrolight to feature 16 M2.5 threaded holes through which it could also be fastened to the 8U structural frame of the satellite using 16 M2.5 countersunk screws. This addition provides better mechanical stability of the amplifier and an additional path for the conductive transfer of the dissipated heat. Figure 4 presents an overview of the attachment of the ATLAS amplifier assembly to the primary 8U structural frame and the -Y external aluminum panel of the CubeSat ERMIS-3.

Regarding the PC/104 [22] electronic boards of the satellite's main stack, these are placed on four DIN 976 M3 × 0.5 metric thread stud bolts [23] and are held in place using round spacers made of nickel-plated brass. The high thermal conductivity of the brass spacers allows for the creation of an effective conductive heat transfer path between the PC/104 boards and the satellite's structure. Other components of the satellite that are

characterized by considerable heat dissipation, such as the NanoPower P80 Electrical Power System (EPS) module, the NanoCom Link SX module, or the Atlas FSO module are mounted directly on the aluminum frame of the satellite using M2.5 countersunk screws. In this way, the satellite structure can act effectively as a heat sink for these components. In terms of thermal control, the aluminum alloys (AA7075, AA6082, and AA5005) used in the primary structure, secondary structural elements, and external cover panels of ERMIS-3 also facilitate the distribution of thermal energy to the entire body of the satellite as a result of their high thermal conductivity, and in this way prevent localized overheating phenomena. In general, ERMIS-3 relies mainly on passive thermal control measures, with the only exception being the two NanoPower BP8 Li-ion battery packs, which are equipped with a 6 W electrical heating element each, to ensure that the sixteen 18,650 Li-ion cells of the satellite remain above their minimum allowable temperature limits when in cold conditions.

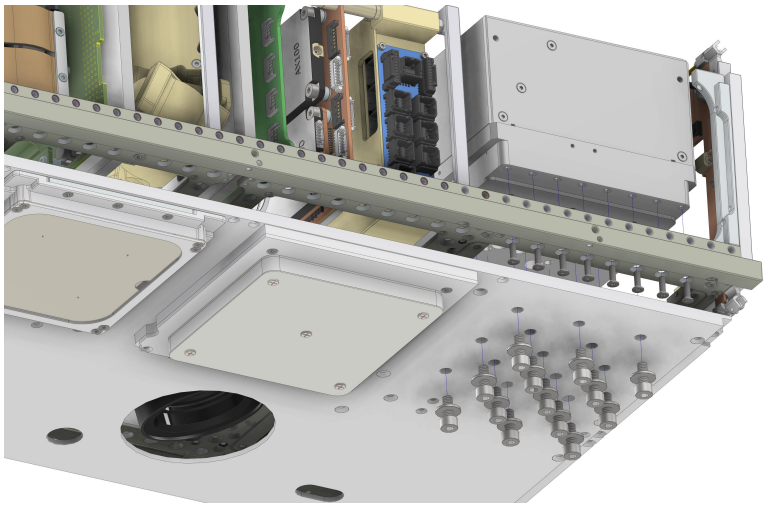

Figure 4. A CAD rendering of ERMIS-3 showing the mounting of the ATLAS amplifier assembly on the 8U CubeSat structure and the -Y external aluminum panel of the satellite.

3. The Thermal Environment of LEO

During its mission, the CubeSat ERMIS-3 is subjected to the demanding thermal environment of LEO, which is characterized by periods of intense heat when the satellite is exposed to the direct solar flux during the sunlit portion of the orbit, followed by periods of intense cold when it is located in the eclipse portion of its orbit. Before proceeding to the thermal modeling and analysis of ERMIS-3, the present section is dedicated to the presentation of some fundamental information about the thermal environment of LEO.

Every satellite or spacecraft that is in orbit around the Earth is subjected to three external heat sources along with an internal one, which is the heat that is generated by the operation of its subsystems. These three external heat sources include direct solar radiation (also commonly referred to as direct solar flux), albedo radiation, and long-wavelength IR radiation that is emitted by the Earth. Of these, the direct solar flux is by a large extent the most prominent external heat source for a spacecraft operating in Earth orbit. The intensity of the solar flux does not remain constant during the calendar year, as it varies due to the constantly changing distance that separates the Earth from the Sun; more specifically, during the Summer Solstice, the Earth is close to its Aphelion, and the solar flux intensity is close to its minimum value of 1322 W/m^2. Similarly, during the Winter Solstice, the Earth is close to its Perihelion, and therefore the solar flux approaches its maximum value of 1414 W/m^2. Regarding the spectral distribution of the solar flux, it consists of approximately 7% ultraviolet, 46% visible, and 47% near (short-wavelength) infrared [24].

The second external heat source, albedo radiation (also referred to as albedo flux), encompasses the portion of solar radiation which indirectly reaches the surfaces of a spacecraft after being reflected off the surface of the planet towards space. The intensity of albedo radiation is usually expressed through a dimensionless measure defined as the albedo fraction (A_F), which is the fraction of the original incident to the Earth solar radiation that is reflected back into space. The value of the albedo fraction ranges between 0 and 1. Usually, the reflectivity of the Earth is greater over its continental regions compared to its oceanic masses. Furthermore, due to the high reflectivity exhibited by clouds, snow, and ice, albedo radiation intensity tends to increase with increasing latitude, reaching its maximum over the polar regions of the Earth, while also reaching high values over areas that are extensively covered in clouds. Furthermore, the intensity of the albedo radiation that reaches a spacecraft is also dependent on its orbital altitude, with satellites located in LEO facing higher albedo fluxes compared to satellites located in higher altitude orbits. Similarly, satellites located in high inclination orbits, such as polar or Sun-synchronous orbits, will be exposed to higher albedo radiation environments compared to equatorial ones due to the high reflectivity of the Earth's ice-covered polar regions. These significant variations in albedo radiation introduce considerable uncertainty, making the accurate selection of albedo values for a thermal analysis complicated, and therefore ranges of the albedo fraction are used to express both its higher and lower possible values for each orbit. As it is essentially solar radiation, albedo radiation has the same spectral distribution as the direct solar flux [24]. If a simplified model of a satellite is considered, as specified in [12], then the total rates at which direct solar ($\dot{Q}_{Solar}$) and albedo ($\dot{Q}_{Albedo}$) radiation are absorbed by the surfaces of the satellite can be calculated using Equation (1) and Equation (2), respectively.

$$\dot{Q}_{Solar} = \alpha A_S S \cos\theta \tag{1}$$

$$\dot{Q}_{Albedo} = \alpha A_S A_F S F_{Earth \to Satellite} \tag{2}$$

where α is the solar absorptivity of the satellite's surfaces, A_S is the surface area of the satellite in m^2, θ is the incident angle between the surface's normal vector and the solar vector in °, S is the intensity of the direct solar flux in W/m^2, A_F is the albedo fraction and $F_{Earth \to Satellite}$ is the view factor between the surfaces of the Earth and the surface of the satellite, ranging from 0 to 1 depending on the orientation of the surfaces.

The part of the direct solar radiation hitting the Earth that is not reflected as albedo radiation is absorbed by the surface of the planet, leading to it reaching an effective thermal balance at approximately 255 K. Therefore, like any real object with a temperature that is higher than 0 K, the Earth also emits thermal radiation. Because the temperature of the Earth is considerably lower than that of the Sun, the radiation emitted by it towards space is IR radiation of longer wavelengths. Like in the case of albedo, the IR radiation emissions of the Earth vary greatly from region to region. This can mainly be attributed to climate factors, such as local temperature or potential cloud cover. More specifically, the highest values of Earth IR radiation are expected to occur over the hottest regions of the planet, such as tropical and desert regions, and will decrease progressively with increasing latitude, reaching their minima over the polar regions of the planet, which are the coldest ones. Furthermore, intense cloud cover can also affect the intensity of the IR radiation emitted by the Earth as clouds can decrease the amount of IR radiation that is emitted by the surface of the planet that eventually reaches space. Therefore, in the thermal design and analysis of satellites, similar to albedo, maximum and minimum orbit-averaged values can be used for the Earth IR radiation as well [24]. Some detailed models that provide information about the variation of the Earth IR and albedo values over the course of the calendar year, as well as the effect of latitude, orbital altitude, inclination, and ascending node location

on these values are presented in [25,26]. If a simplified model of a satellite is considered again, the rate of Earth IR radiation that is absorbed by the surface of the satellite ($\dot{Q}_{Earth,IR}$) is given by Equation (3) [12].

$$\dot{Q}_{Earth,IR} = \varepsilon A_S S_{Earth,IR} F_{Earth \to Satellite} \quad (3)$$

where ε is the IR emissivity of the satellite's surfaces, A_S is the surface area of the satellite in m^2, $S_{Earth,IR}$ is the intensity of the IR radiative flux that is emitted by the Earth in W/m^2, and $F_{Earth \to Satellite}$ is the view factor between the surface of the Earth and the surfaces of the satellite, ranging from 0 to 1 depending on the orientation of the surfaces.

Therefore, the combined rate at which the satellite's surfaces absorb heat from all three external heat sources ($\dot{Q}_{In}$) may be calculated by using Equation (4).

$$\dot{Q}_{In} = \dot{Q}_{Solar} + \dot{Q}_{Albedo} + \dot{Q}_{Earth,IR} \quad (4)$$

The satellite absorbs thermal energy from all three external heat sources ($\dot{Q}_{In}$) and part of this heat, along with part of the heat that is generated by the satellite's subsystems ($\dot{Q}_{Generated}$), is stored by the satellite ($\dot{Q}_{Stored}$) leading to changes in its temperature, while another part is radiated towards space ($\dot{Q}_{Out}$), which acts as a heat sink to which it can reject excess heat in the form of IR radiation. The relationship between the temperature change rate of the satellite and the rate at which thermal energy is absorbed or rejected by it ($\dot{Q}_{Stored}$) is given by Equation (5). From this equation, it is obvious that the higher the mass and specific heat capacity of the satellite, the higher its thermal inertia, meaning that a greater heating or cooling rate is needed in order to change its temperature by the same amount. It is for this reason that small satellites like CubeSats are much more sensitive to changes in the thermal environment of space compared to their larger counterparts. Finally, the heat that is eventually emitted by the satellite in the form of IR radiation towards space ($\dot{Q}_{Out}$) is given by Equation (6). It should be kept in mind that both the satellite and the Earth emit IR radiation of comparable wavelengths. This is expected as both bodies have absolute temperatures of comparable levels, especially when compared to the temperature of the Sun, which is thousands of degrees hotter. For this reason, contrary to solar radiation, the Earth IR radiative heat loads that are incident to a spacecraft cannot be reflected away from its surfaces through the use of thermal control coatings that exhibit low IR emissivity (ε), since the same coatings would also prevent the rejection of excess heat from the satellite, which is of the same spectral range, eventually leading to an overheating situation [12,24].

$$\dot{Q}_{Stored} = \rho V c_p \frac{\partial T}{\partial t} \quad (5)$$

where ρ is the average density of the satellite in kg/m^3, V is the volume of the satellite in m^3, c_p is the satellite's average specific heat capacity at constant pressure in $J/kg \cdot K$, T is the absolute temperature of the satellite in K, and t is the time in seconds.

$$\dot{Q}_{Out} = \dot{Q}_{Radiated} = \varepsilon \sigma A_S F_{Satellite \to \mathrm{Space}} \left(T_{Surface}^4 - T_{Space}^4 \right) \quad (6)$$

where ε is the IR emissivity of the satellite's surfaces, σ is the Stefan–Boltzmann constant which is equal to $5.670374419 \times 10^{-8}\ W/m^2 \cdot K^4$, A_S is the surface area of the satellite in m^2, $F_{Satellite \to \mathrm{Space}}$ is the view factor between the surface of the satellite and space, which ranges from 0 to 1 (the view factor has a value that is equal to 1 in the cases where a satellite's surface in question has an unimpeded view of space), $T_{Surface}$ is the absolute temperature of the satellite's surfaces in K, and T_{Space} is the absolute temperature of space in K.

In conclusion, a satellite orbiting Earth reaches thermal balance when the heat generated by its subsystems and the heat absorbed by its surfaces from the external heat sources are equal to the heat that is stored in the body of the satellite and the heat that it rejects towards space, as shown by Equations (7) and (8). Figure 5 provides a simplified visualization of the different external heat loads acting on a satellite in Earth orbit.

$$\dot{Q}_{In} + \dot{Q}_{Generated} = \dot{Q}_{Stored} + \dot{Q}_{Out} \tag{7}$$

$$\dot{Q}_{Solar} + \dot{Q}_{Albedo} + \dot{Q}_{Earth,IR} + \dot{Q}_{Generated} = \dot{Q}_{Stored} + \dot{Q}_{Out} \tag{8}$$

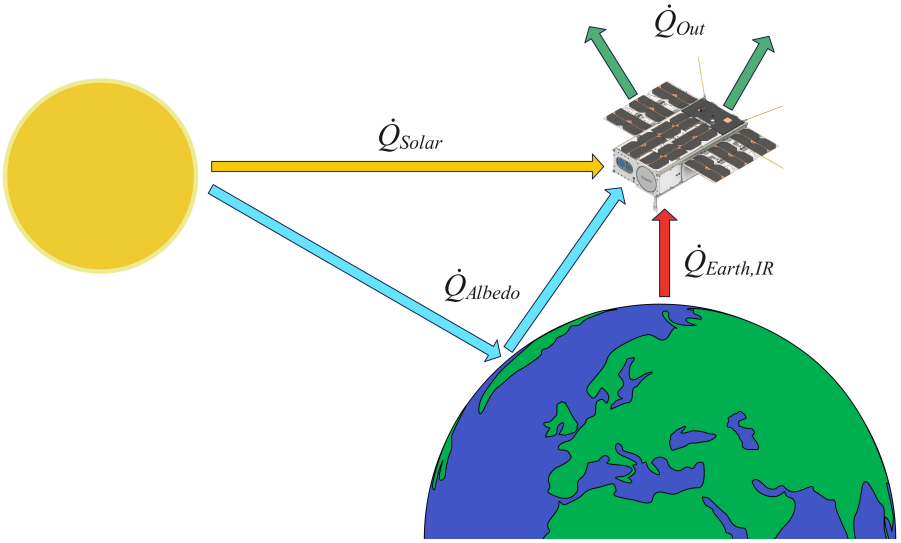

Figure 5. A simplified overview of the different heat loads that act on a satellite that operates in Low Earth Orbit (LEO).

An important quantity in the thermal analysis of satellites is the orbit's beta (β) angle. The β angle is defined as the minimum angle formed between the orbital plane and the solar vector, and is described by Equation (9) [24].

$$\beta = \sin^{-1}\left(\cos\delta_s \sin RI \sin\left(\Omega - \Omega_s\right) + \sin\delta_s \cos RI\right) \tag{9}$$

where δ_s is the declination of the Sun (which reaches its seasonal extremes of ±23.45° at the solstices), RI is the orbital inclination, Ω is the right ascension of the orbit's ascending node, which is directly related to the spacecraft's Local Time of the Ascending Node (LTAN), and Ω_S is the right ascension of the Sun. All the aforementioned values are measured in °.

4. Creating the Thermal Model of the CubeSat ERMIS-3

As of the beginning of its mission, ERMIS-3 is located in an SSO with an apogee altitude of 516.43 km, a perigee altitude of 501.33 km, an inclination of 97.45°, and an LTAN in the 14:00:00 + 60 min range. It was launched to this orbit via SpaceX's (Space Exploration Technologies Corp., Starbase, TX, USA) Transporter-16 dedicated rideshare mission, which took place on 30 March 2026. However, by the time this thermal analysis took place, the final orbit of Transporter-16 had not yet been decided, and an orbit with LTAN located anywhere between 13:00:00 and 15:00:00 was possible. For this reason, an orbit with LTAN 15:00:00 was used as the basis of the "Hot" cases due to its shorter eclipse duration, while an orbit with LTAN 13:00:00 was used in the "Cold" cases of the thermal analysis. These conditions were not redefined when the actual LTAN of Transporter-16 became known as they represent more extreme (and therefore more conservative) cases than the actual

mission's LTAN, and in that way add another layer of safety margin to the satellite's thermal design towards both the hot and the cold ends.

The orbital thermal environment principles discussed in the previous section were applied for the creation of an FE thermal model of ERMIS-3, using the Orbital Thermal Loads User Interface of the Heat Transfer Module add-on to COMSOL Multiphysics (software version 6.1). The first step in the creation of the thermal model of the satellite was to collect all relevant thermal and physical properties of the primary materials that make up the satellite's subsystems. These properties include density (ρ), thermal conductivity (k), and specific heat capacity at constant pressure (c_p). An overview of the thermal and physical properties of the materials that were utilized in the thermal model of ERMIS-3 is provided in Table 1. This information has been collected by reviewing relevant literature, such as handbooks and published papers, as well as from online material databases. In a manner similar to the thermal and physical properties presented in Table 1, an overview of the optical properties, namely the solar absorptivity (α) and the IR emissivity (ε) of all the relevant surfaces of ERMIS-3 is presented in Table 2. As the optical properties have a significant impact on the thermal balance of the satellite, the use of values that are as accurate as possible is crucial. Therefore, values reported by NASA, values reported in spacecraft thermal design and control handbooks, as well as values presented in previously published works on completed CubeSat missions were utilized for most of the satellite's modeled surfaces. In addition, online databases were also consulted.

Table 1. The thermal and physical properties of the primary materials used in the thermal FE model of the CubeSat ERMIS-3.

Material	k (W/m · K)	c_p (J/kg · K)	ρ (kg/m^3)	Source
Aluminum 7075 (UNS A97075)	121.20	961.20	2770.00	[27]
Aluminum 6082 (UNS A96082)	160.00	900.00	2700.00	[28]
Aluminum 5083 (UNS A95083)	117.70	961.20	2770.00	[27]
Aluminum 5005 (UNS A95005)	206.00	961.20	2770.00	[27]
Aluminum 2024 (UNS A92024)	121.20	921.60	2770.00	[27]
Stainless Steel 304 (UNS S30400)	16.30	504.00	8030.00	[27]
Stainless Steel 316 (UNS S31600)	16.30	504.00	8030.00	[27]
Ti-6Al-4V (UNS R56400)	7.30	572.40	4430.00	[27]
Copper (UNS C11000)	391.20	385.20	8860.00	[27]
Brass (UNS C38500)	122.90	378.00	8580.00	[27]
Phosphor Bronze (UNS C51000)	69.20	378.00	8860.00	[27]
Alumina (ASTM D2442 Type II)	19.00	900.00	3700.00	[29]
Glass (Fused Quartz)	1.50	712.80	2210.00	[27]
Polyimide (Kapton)	1.13	1130.00	1420.00	[30]
FR4 Glass-Fiber Epoxy Laminate	0.29	1150.00	1800.00	[31]
Polycarbonate	0.19	1670.00	1350.00	[32]
Polyphenylene Sulfide (unfilled)	0.25	1000.00	1300.00	[33]
Gallium Arsenide (GaAs)	32.90	334.80	5260.00	[27]
Germanium (Ge)	60.60	324.00	5260.00	[27]
Indium Gallium Phosphide (InGaP)	5.30	370.00	4475.00	[34,35]
Lithium-ion Cells (Averaged)	30.40/0.20 *	1720.00	2362.00	[36]

* In this case, the 30.40 W/m·K value refers to the axial direction of the cylindrical 18,650 Li-ion cell while the 0.20 W/m·K value refers to its radial direction.

Table 2. An overview of the optical properties used in the surfaces of the thermal FE model of the CubeSat ERMIS-3.

Material/Coating	Optical Property		Source
	α	ε	
Aluminum–Anodized Clear	0.43	0.67	[37]
Aluminum–Anodized Black	0.70	0.86	[37]
Aluminum 7075–Anodized Clear	0.68	0.82	[37]
Aluminum 7075–Hard Anodized	0.83	0.87	[37]
Aluminum Tape	0.21	0.04	[38]
Kapton Film	0.38	0.67	[37]
SurTec® 650	0.34	0.05	[39]
Stainless Steel Machined	0.47	0.14	[37]
Nickel-Plating	0.39	0.07	[37]
Electroplated Gold	0.23	0.03	[37]
Copper	0.30	0.03	[40]
Titanium	0.40	0.55	[40]
Dark PCB Surfaces	0.77	0.89	[41]
White PCB Surfaces	0.49	0.90	[41]
Solar Cells	0.93	0.85	[41]
Plastic	–	0.90	[42]
Black Paint	0.96	0.91	[40]
Glass	0.15	0.84	[43]

In many locations of the satellite, heat is transferred through contact joints between different individual components that have either been fused together using adhesives or have been connected via the use of screws and/or spacers. Examples of such joints include the contacts that exist between the external aluminum panels and the primary aluminum structure of the satellite, the contacts between electronic boards and brass or aluminum spacers that are used for their mechanical support, the contacts that exist in the interior of hinge mechanisms that connect deployable components (such as the deployable solar arrays, the deployable Ultra-High Frequency (UHF) antenna monopoles, and the deployable magnetometer in the case of ERMIS-3) with the part of them that remains fixed to the main body of the satellite, as well as the contacts between electronic chips and their aluminum heat sinks and/or motherboard Printed Circuit Boards (PCBs). The exact amount of heat that is transferred through contact joints is quantified by a property defined as the heat-transfer coefficient, or the thermal contact conductance which is the product of the heat-transfer coefficient and the contact area, as expressed by Equation (10) [44].

$$C = h_C A \tag{10}$$

where C is the thermal contact conductance in W/K, h_C is the contact joint's heat-transfer coefficient in $W/m^2 \cdot K$, and A is the contact area of the joint in m^2.

The exact value of the thermal contact conductance between two discrete objects that are in contact with each other is a function of different parameters, such as the thermal conductivity of the two materials involved, the amount of pressure that is applied on the joint, as well as the roughness and cleanliness of the object surfaces. Furthermore, the deformation behavior of the two mediums in contact is also of significant importance to the thermal contact conductance levels [44]. Therefore, various models that can be used to predict the value of the thermal contact conductance of a joint have been proposed over the years, such as the Cooper–Mikic–Yovanovich model [45], the Mikic model [46], or the Sridhar-and-Yovanovich model [47], among various others. In most cases, the accurate calculation of the actual thermal contact conductance values of a satellite assembly using

detailed prediction models such as the aforementioned ones requires the performance of experimental measurements on the flight hardware, something that was not possible during the preparation and execution of this analysis, which took place before the assembly and integration of the satellite. Therefore, for the modeling of threaded connections (bolted interfaces) between different components, such as aluminum panels, structural brackets, and structural rings, and the main frame of the satellite or the contacts between boards and spacers, the thermal contact conductance was calculated based on empirical relations by utilizing information such as the tightening torque, as well as the size and number of screws utilized in each connection [12,44,48]. Furthermore, for contacts between fused or soldered electronic components such as integrated circuit – PCB contact pairs, the utilized thermal contact conductance values were based on data collected by review of relevant published literature such as the 0.038 W/K value reported in [8]. In this regard, Table 3 summarizes some of the contact joint heat-transfer coefficient values assigned to key thermal interfaces of the FE thermal model of ERMIS-3.

Table 3. The contact joint heat-transfer coefficient values assigned to some key thermal interfaces of the ERMIS-3 FE thermal model.

Thermal Interface Pair	h_C (W/m^2·K)
-Y Cover Panel–ATLAS Amplifier Assembly	500
ATLAS Amplifier Assembly–8U Frame	3000
ATLAS FSO Assembly–8U Frame	2000 & 2300
NanoPower P80 EPS–8U Frame	2700
NanoPower BP8–8U Frame	4700
PDPU–8U Frame	4700
HyperScape100–Support Brackets	450
HyperScape100–Support Ring	250
-Y Cover Panel–8U Frame	450
Spacer–PC/104 PCB	8000
Daughterboard–Spacers	4000
Spacers–Motherboard PCB	4000
Star tracker–Support Deck	3800

These values were calculated empirically using the number and size of screws connecting the two components in question and the contact area.

A considerable fraction of a CubeSat's total heat dissipation takes place on its individual PCBs due to integrated circuits, processors, capacitors, and resistors contained by those PCBs. In these cases, the body of the PCB represents a means through which the heat generated by its integrated elements or daughterboards eventually flows towards the satellite's structure. Therefore, the correct modeling of their thermal properties is of significant importance to the accuracy of the thermal analysis of the satellite at subsystem level. To simplify the FE thermal model of ERMIS-3 and, therefore, decrease the total computational overhead, the alternating copper and dielectric material layers present inside the real PCBs were not modeled explicitly, and homogeneous geometric equivalent models were used instead. However, to preserve accuracy, these simplified models were assigned effective (spatially averaged) properties based on the ratio of copper to dielectric material contained within each board. More specifically, the following procedure was followed.

First and foremost, it needs to be acknowledged that a CubeSat will feature PCBs that are different both in terms of total thickness, as well as with regard to the exact number and thickness of copper layers contained within them. For example, in CubeSat systems that utilize high currents, such as telecommunication transceivers/antennas and electrical power systems, thicker boards with more copper percentagewise may be used. On the other hand, lower electrical power consumption applications such as sensory instruments

or simple motherboards or daughterboards may use thinner, simpler PCBs with less copper content. Therefore, it was decided to model four different cases of PCB compositions for ERMIS-3. More specifically, "Case 1" where a PCB with a standard total thickness of 1.57 mm contains two external (top and bottom) 17.50 μm and two internal 35.00 μm thick layers of copper, "Case 2" where a PCB with a total thickness of 1.57 mm contains four 35.00 μm-thick layers of copper, "Case 3" where a PCB with a total thickness of 1.57 mm contains two external 17.50 μm and six internal 35.00 μm-thick layers of copper and "Case 4" where a PCB with a total thickness of 2.36 mm contains two external 17.50 μm and 14 internal 35.00 μm-thick copper layers. Detailed illustrations of these four modeled PCB cases are presented in Figure 6. In all these cases, for modeling simplicity, it is assumed that the alternating dielectric material and copper layers are homogeneous and feature the same cross-sectional area, while the existence of smaller traces of copper on the boards was ignored. In these illustrations, the dielectric material layers are symbolized by the green color while the copper layers are the brown ones. The existence of a PCB solder mask on the top and bottom copper layers' surfaces is omitted from the visualizations and the calculations.

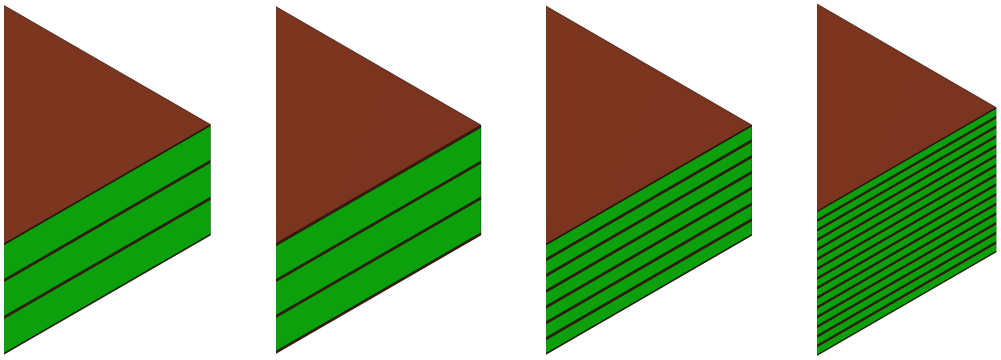

Figure 6. Isometric views of the four different PCB geometric models that were utilized in the modeling of the Printed Circuit Boards (PCBs) of ERMIS-3. (**a**) A board with a total thickness of 1.57 mm containing two external 17.50 μm and two internal 35.00 μm-thick copper layers (Case 1). (**b**) A board with a total thickness of 1.57 mm and four 35.00 μm-thick layers of copper (Case 2). (**c**) A board with a total thickness of 1.57 mm with two external 17.50 μm and six internal 35.00 μm-thick layers of copper (Case 3). (**d**) A board with a total thickness of 2.36 mm containing a total of two external 17.50 μm-thick and 14 internal 35.00 μm-thick layers of copper (Case 4).

On the basis of these assumptions, it is obvious that the layered composition of the PCBs will lead to different effective values regarding their in-plane and out-of-plane thermal conductivities. More specifically, the effective in-plane and out-of-plane thermal conductivities of the homogeneous equivalent PCB model are calculated using a thickness-weighted approach through Equations (11) and (12), which are presented in [12]. Similarly, the effective specific heat capacity of the homogeneous model can be calculated by the mass analogy of the different materials that constitute the boards, as expressed by Equation (13) [12]. Moreover, since dielectric material and copper feature considerably different densities, the effective volume- weighted density of the boards can be calculated using Equation (14).

$$k_{effective,in-plane} = \frac{1}{t}\sum_{i=1}^{n}(k_i t_i) \quad (11)$$

$$k_{effective,out-of-plane} = \frac{t}{\sum_{i=1}^{n}\left(\frac{t_i}{k_i}\right)} \quad (12)$$

$$c_{p_{effective}} = \frac{1}{m}\sum_{i=1}^{n}(m_i c_{p_i}) \quad (13)$$

$$\rho_{effective} = \frac{\sum_{i=1}^{n} m_i}{\sum_{i=1}^{n} V_i} = \frac{\sum_{i=1}^{n} \rho_i V_i}{\sum_{i=1}^{n} V_i} \quad (14)$$

where t is the total thickness of the PCB in m, t_i is the thickness of an individual material layer in m, k_i is the thermal conductivity of each individual material layer in $W/m \cdot K$, m is the total mass of the PCB in kg, m_i is the mass of each material layer in kg, c_{p_i} is the specific heat capacity at constant pressure for each material layer in $J/kg \cdot K$, V_i is the volume of each material layer in m^3, ρ_i is the density of each material layer in kg/m^3, and n is the total number of alternating material layers.

Furthermore, regarding the dielectric material of the PCBs, since ERMIS-3 features both glass-fiber epoxy FR4 laminate and polyimide PCBs, both materials were utilized in the modeling procedure, assigned according to the exact dielectric material of the PCB of ERMIS-3 being modeled. This led to eight distinct PCB modeling cases, all of which are summarized in Table 4, which contains the spatially averaged in-plane and out-of-plane thermal conductivities, as well as the specific heat capacities at constant pressure and the densities of the different PCB models used in the FE thermal simulation model of ERMIS-3.

Table 4. An overview of the effective physical and thermal properties considered in the different PCBs of the CubeSat ERMIS-3.

PCB Layout Case	$k_{in-plane}$ (W/m·K)	$k_{out-of-plane}$ (W/m·K)	c_p (J/kg·K)	ρ (kg/m^3)
Glass-Fiber Epoxy FR4 Laminate PCBs				
1	26.43	0.31	950.55	2272.17
2	35.15	0.32	901.30	2429.55
3	61.29	0.34	785.59	2901.72
4	87.25	0.37	702.77	3370.55
Polyimide Dielectric Material PCBs				
1	27.22	1.21	899.85	1917.58
2	35.91	1.24	847.56	2083.44
3	62.00	1.34	731.02	2581.02
4	87.90	1.45	652.62	3075.08

The same procedure was also utilized for the calculation of the effective thermal and physical properties of the satellite's solar cells as well. More specifically, ERMIS-3 is equipped with a total of 40 individual solar cells between its single GomSpace NanoPower Modular Solar Panel (MSP) B-4-4 [49] and the two NanoPower Deployable Solar Panel (DSP) [50] arrays. The cells of these arrays are the CTJ-LC Triple-Junction InGaP/GaAs/Ge cells which are manufactured by CESI S.p.A. (Milan, Italy) for space applications and feature a Beginning-of-Life (BOL) efficiency of 28.30% at a temperature of 25 °C [51]. Since the exact thicknesses of the InGaP, GaAs, and Ge layers of these cells are not known, the layout that is presented in [52] was used for the modeling procedure where the considered cell layout is 0.80 μm InGaP, 2.00 μm GaAs, and 175.00 μm Ge, while the effect of the tunnel junctions is omitted from the thermal model of the cells due to their small thickness. Therefore, the effective averaged thermal and physical properties of the homogeneous model representing the solar cells of ERMIS-3 as calculated using Equations (11)–(14) are

presented in Table 5. A similar philosophy was also used for the calculation of all the effective thermal and physical properties that were utilized on the simplified thermal models of all other individual components of ERMIS-3.

Table 5. The effective thermal and physical properties considered in the modeling of the Triple-Junction InGaP/GaAs/Ge solar cells of ERMIS-3.

Material	$k_{in-plane}$ (W/m·K)	$k_{out-of-plane}$ (W/m·K)	c_p (J/kg·K)	ρ (kg/m^3)
Solar Cell (Effective)	60.04	57.36	324.30	5256.47

In a similar manner, the optical properties of the satellite's internal and external surfaces that are comprised of two or more different exposed materials and/or surface coatings with different IR emissivity (ε) and solar absorptivity (α) can also be averaged into an effective IR emissivity and an effective solar absorptivity based on the fraction of the surface each material covers. More specifically, the effective IR emissivity ($\varepsilon_{effective}$) of a surface that is made up of multiple different materials can be calculated using Equation (15), while for the calculation of the effective solar absorptivity ($\alpha_{effective}$) Equation (16) can be used in the same manner [12]. For example, in the case of ERMIS-3 this area-averaged approach was used to model the optical properties of simplified surfaces that in the detailed model of the satellite are constituted by two or more materials. For example, in cases of aluminum casings that also feature protruding connectors made of polymer materials or in cases where a primarily aluminum surface also features certain integrated PCBs.

$$\varepsilon_{effective} = \sum_{i=1}^{n} \varepsilon_i \frac{A_i}{A} \tag{15}$$

$$\alpha_{effective} = \sum_{i=1}^{n} \alpha_i \frac{A_i}{A} \tag{16}$$

where A is the total surface area of the geometric surface in question in m^2, n is the total number of different materials and coatings present on the surface, A_i is the surface area of each individual material/coating in m^2, α_i is the solar absorptivity of each individual material/coating, and ε_i is the IR emissivity of each individual material/coating.

All the active electrical and electronic systems present onboard ERMIS-3 dissipate heat during their operation. Therefore, this dissipated thermal energy also needs to be included in the numerical simulation model of the satellite. The total amount of heat dissipated by the subsystems of the satellite may vary greatly with each operating mode the satellite finds itself in, as certain subsystems that are active in one mode of operation of the satellite may be deactivated in another, leading to different combinations of active systems that need to be considered. This means that under certain combinations of extreme orbital thermal environmental conditions and subsystem heat dissipation, sections of the satellite could face the danger of overheating, whereas in other cases some components of the satellite could approach their minimum allowable temperature limits. For this reason, multiple operational cases of the satellite were simulated to ensure that ERMIS-3 is capable of surviving and successfully operating in the thermal environment of LEO. For most components, no explicit heat dissipation values were available. Therefore, to calculate the heat dissipated by each component in a manner that is as representative and as accurate as possible, the calculated power consumption of each component was considered and paired with efficiency numbers that were retrieved from relevant bibliography for similar systems, or efficiency values found in component datasheets. This way, the amount of electrical power consumed by each component that is dissipated in the form of heat was calculated

in an approximate, but at the same time well-informed manner. Table 6 presents the heat dissipation values that were considered for the individual components of ERMIS-3 during the presented thermal simulations. Note that components listed with a heat dissipation of 0.000 W are inactive during the specific simulated operational mode.

Table 6. The heat dissipated by the subsystems of ERMIS-3 during the safe mode, Sun-tracking mode, hyperspectral imaging mode, and laser-optical communication link mode of the satellite respectively.

Component	**Dissipated Heat per Mode of Operation (W)**			
	Safe Mode	**Sun-Tracking Mode**	**Hyperspectral Imaging Mode**	**Laser-Optical Link Mode**
On-Board Computer (OBC) and Telemetry, Tracking & Command System (TT&C)				
NanoMind A3200	0.250	0.250	0.250	0.250
NanoCom AX100	0.500	0.500	0.500	0.500
NanoCom ANT-6F UHF	0.010	0.010	0.010	0.010
Attitude Determination and Control System (ADCS)				
Reaction Wheels	0.000	0.250	0.250	0.250
Magnetorquers	0.020	0.100	0.100	0.100
CubeComputer	0.200	0.200	0.200	0.200
Fine Sun Sensor	0.100	0.100	0.100	0.100
Earth Horizon Sensor	0.200	0.200	0.200	0.200
Compact Magnetometer	0.050	0.050	0.050	0.050
Deployable Magnetometer	0.050	0.050	0.050	0.050
PST3S-H2 Star Tracker	0.000	0.000	$(0.700)^{\S}$	$(0.700)^{\S\S}$
Global Navigation Satellite System (GNSS)				
OEM719 GNSS Receiver	0.000	1.300	1.300	1.300
TW1322 GNSS Antenna	0.000	0.030	0.030	0.030
Electrical Power System (EPS)				
NanoPower BP8 (Li-ion cells)	$(\dot{Q}_{\text{Bat.}})^{\dagger} + \dot{Q}_{\text{Heater}}$	$(\dot{Q}_{\text{Bat.}})^{\dagger} + \dot{Q}_{\text{Heater}}$	$(\dot{Q}_{\text{Bat.}})^{\dagger} + \dot{Q}_{\text{Heater}}$	$(\dot{Q}_{\text{Bat.}})^{\dagger} + \dot{Q}_{\text{Heater}}$
NanoPower P80 EPS (PMU)	0.500	0.500	0.500	0.500
NanoPower P80 EPS (ACU)	$(0.300 + \dot{Q}_{\text{ACU}})^{\dagger}$	$(0.300 + \dot{Q}_{\text{ACU}})^{\dagger}$	$(0.300 + \dot{Q}_{\text{ACU}})^{\dagger}$	$(0.300 + \dot{Q}_{\text{ACU}})^{\dagger}$
NanoPower P80 EPS (PDU)	$(0.450 + \dot{Q}_{\text{PDU}})^{\dagger}$	$(0.450 + \dot{Q}_{\text{PDU}})^{\dagger}$	$(0.450 + \dot{Q}_{\text{PDU}})^{\dagger}$	$(0.450 + \dot{Q}_{\text{PDU}})^{\dagger}$
Stack Breakout PCB	0.013	0.043	0.043	0.043
Communication System (COMM)				
NanoCom Link SX	0.000	0.000	0.000	0.000
NanoCom ANT2150	0.000	0.000	0.000	0.000
NanoCom ANT8250	0.000	0.000	0.000	0.000
Payload				
ATLAS FSO Assembly	0.000	0.000	0.000	$(1.000 + 7.100)^{\S\S}$
ATLAS Amplifier Assembly	0.000	0.000	0.000	$(21.900)^{\S\S}$
HyperScape 100 Imager	0.000	0.000	$(4.000 + 3.750)^{\S}$	0.000
NanoMind HP MK3 (PDPU)	0.000	0.000	$(2.000 + 2.000)^{\S}$	$(2.000 + 2.000)^{\S\S}$

† The detailed heat dissipation profiles for the ACU, PDU, and the battery packs of the EPS of ERMIS-3 are presented in Figure A1 of Appendix A.1. § The detailed heat dissipation profiles corresponding to these components in the hyperspectral imaging scenario are presented in Figure A2a of Appendix A.1. §§ The detailed heat dissipation profiles corresponding to these components in the laser-optical link scenario are presented in Figure A2b of Appendix A.1.

Of the multiple different operational modes of ERMIS-3, four are presented in this work. More specifically, these are the safe mode, the Sun-tracking mode, the hyperspectral

imaging mode, and the laser-optical communications mode. Being the modes of operation with the lowest heat dissipation, the safe mode and Sun-tracking mode cases were combined with the "Cold" orbital scenario in order to simulate the coldest possible scenarios the satellite may find itself in. On the other hand, the hyperspectral imaging mode and the laser-optical communications mode cases represent two of the modes of operation with the highest heat dissipation and are therefore combined with the "Hot" orbital scenario to simulate the hottest possible scenarios the satellite may need to operate in. All the results that are presented for these cases cover a period of 11 full orbits. For the two simulations covering the hyperspectral imaging and the laser-optical communications modes of operation, the mission-specific payloads of the satellite are active only during two specific orbits, to represent realistic duty cycles, while for the remaining orbits of these simulations, ERMIS-3 operates in Sun-tracking mode to allow for battery charging.

To simplify the modeling procedure and to optimize computational resource use, the heat dissipation of components that remain active steadily during the satellite's nominal operations was modeled in an orbit-averaged manner, represented by an average value that remains constant throughout the entire simulated case. This approach is best suited for components that do not exhibit significant heat dissipation fluctuations and/or their heat dissipation always remains at low and moderate levels. Examples of such systems include the satellite's Onboard Computer (OBC), the ADCS sensors and actuators, as well as the Power Management Unit (PMU) of the satellite. The NanoCom AX100 transceiver module always remains active during the simulated cases; however, on average it operates in receive mode for 90% of the orbit and in transmission mode for 10%, when passing over a ground station. As a result, to simplify its modeling, a stable, weighted heat dissipation of 0.500 W was considered for this component as well.

Conversely, mission-critical components with considerable heat dissipation such as the HyperScape100 hyperspectral imager, the ATLAS laser-optical communications terminal, the PDPU, the Power Distribution Unit (PDU), or the Array Conditioning Unit (ACU) of the EPS, are modeled in a more explicit and dynamic manner, using time-variant heat dissipation profiles. This modeling approach allows for the more accurate and realistic thermal simulation of these components as it also considers the individual subsystem's and the satellite's thermal inertia, leading into more representative results. Regarding the heat dissipation of the ATLAS FSO and amplifier assemblies, relevant values were provided by Astrolight. More specifically, in the present analysis, conservative heat dissipation values equal to 8.10 W for the FSO assembly and 21.90 W for the amplifier assembly were utilized, which correspond to the absolute maximum predicted heat dissipation values of these components. However, during nominal operations of the ATLAS terminal, more modest heat dissipation values of approximately 4.00 W for the FSO assembly and 15.00 W for the amplifier assembly are expected.

In order to further enhance the accuracy of the FE thermal model of ERMIS-3, many aspects of the heat that is dissipated by its Electrical Power System (EPS), such as the battery pack electrical heating elements, the heat generated by the ACU during electrical power generation and conditioning, the heat generated by the PDU during subsystem activation and operation, as well as the efficiency of the Li-ion cells during the charge and discharge phases were modeled in a time-varying, semi-dynamic manner rather than being represented only by orbit-averaged values. The exact procedure that was followed is presented in the following paragraphs.

The first step for this approach was the calculation of the incident solar flux converted into electrical power by the satellite's solar cells. During the simulation, an integration of the solar flux (both direct and albedo) over the total area of the solar cells is performed. The resulting integral is then multiplied by the conversion efficiency of the solar cells,

providing the simulation model with a system variable representing the total instantaneous amount of solar radiation that is eventually converted into electrical power ($P_{Generated}$), as expressed by Equation (17). To realistically model the conversion efficiency of the solar cells, performance drops relative to the reported 28.30% BOL value must also be considered. More specifically, in real conditions, the efficiency of the solar cells deviates from the ideal performance due to elevated solar cell operational temperatures from Sun exposure [53,54] and also due to the progressive degradation of the solar cells as a result of the effects of the space environment [55]. Therefore, to determine the most appropriate efficiency values for the "Cold" and "Hot" simulated thermal scenarios of ERMIS-3, a multi-step adjustment procedure was implemented.

$$P_{Generated} = \eta_{Cell} \int_{A_{Cell}} S_{Incident}\, dA_{Cell} \tag{17}$$

where η_{Cell} is the conversion efficiency of the solar cells, $S_{Incident}$ is the solar flux (both direct and albedo) that is incident to the solar cells of ERMIS-3 in W/m^2, and A_{Cell} is the total surface area of the solar cells that is available for electrical power generation in m^2.

First, a temperature-dependent efficiency reduction coefficient of 0.059%/°C (or 0.00059/°C) was adopted, a value that is consistent with data reported by [53], a work that discusses similar photovoltaic cells. An iterative convergence study was then conducted using the satellite's FE thermal model to effectively capture the coupled thermo-electrical behavior of the solar cells. In this procedure, candidate efficiency values were systematically evaluated until the FE-calculated temperatures converged with the efficiencies that produced them. This convergence study demonstrated that during the sunlit portion of the orbit, the average solar cell temperature rises sharply, reaching levels of approximately 50.00 °C during the "Cold" cases and 57.00 °C during the "Hot" ones. These temperatures yielded baseline conversion efficiencies of 26.83% and 26.41%, respectively. Finally, to ensure a high degree of realism and conservatism, these calculated baseline efficiency values were adjusted downward to account for additional, non-thermal losses. Namely, for the "Cold" cases, the efficiency was fixed at 26.50% to incorporate manufacturing defects and imperfections. For the "Hot" cases, a larger reduction down to 25.50% was applied to account for both manufacturing defects, and long-term degradation due to the exposure of the solar cells to the environment of space. This approach, apart from improving the accuracy and realism of the FE thermal model of the EPS, also provided a reliable means by which to calculate the electrical power generated across the various operational modes of ERMIS-3, thereby forming the basis for the electrical power generation simulations that were performed in the preliminary and intermediate design stages of the project.

Since a fraction of the solar radiation incident on the solar cells of ERMIS-3 is converted into electrical power, it does not contribute directly to the radiative heating of the satellite and must be subtracted from the FE thermal model to satisfy the principle of energy conservation. In the model, this was implemented by defining an outward heat flux boundary condition on the surface of the solar cells, which effectively acts as a negative heat source with a magnitude matching the generated electrical power per unit area, thereby counteracting an identical portion of the incident solar flux.

Continuing with the thermal modeling of the satellite's EPS, the ACU of the NanoPower P80 EPS module regulates and optimizes the electrical power generated by the solar arrays of ERMIS-3. This component dissipates heat due to its operational electrical power consumption and, primarily, due to the energy losses within its Maximum Power Point Tracking (MPPT) charge controller elements during power regulation. Following a conservative modeling approach, it was assumed that these electrical energy losses are entirely in the form of dissipated thermal energy. Based on literature regarding similar MPPT

systems reporting efficiencies in the 88.9–94.08% range [56], a representative efficiency of 90% was assigned to the ACU of the ERMIS-3 FE thermal model. As a result, 10% of the electrical power generated by its solar arrays is eventually dissipated within the ACU as conversion losses in the form of heat ($\dot{Q}_{ACU}$), as expressed by Equation (18).

$$\dot{Q}_{ACU} = (1 - \eta_{ACU}) P_{Generated} \tag{18}$$

where η_{ACU} is the efficiency considered for the ACU and $P_{Generated}$ is the electrical power generated by the satellite's solar arrays in W.

To simulate the heat dissipation that occurs during electrical power distribution in the EPS's PDU in a realistic manner, a similar methodology was adopted. More specifically, apart from heating due to the current it consumes for its operation, the PDU also features significant heat dissipation during the supply of electrical power to each component of the satellite. The PDU features a variety of different electrical power distribution channels, each capable of providing a different voltage. Therefore, the reported efficiencies of the power distribution channels can be used to calculate the dissipated heat with considerable accuracy. Consulting the datasheet of the GomSpace NanoPower P80 EPS [57], the efficiencies of the 3.3 V, 5 V, and 12 V power distribution channels were approximated at 90%, 93%, and 95% respectively. Assuming that the losses are entirely in the form of heat, thermal dissipation losses of 10%, 7%, and 5% were considered respectively, depending on the exact power distribution channel utilized by each subsystem. For subsystems powered by unregulated battery power (V_{Bat}), the PDU was assigned an even lower baseline loss of 1%. Thus, the total heat dissipated by the PDU of ERMIS-3 ($\dot{Q}_{PDU}$) was modeled using Equation (19).

$$\dot{Q}_{PDU} = \sum_{i=1}^{n} P_{Load,i} \frac{(1 - \eta_{PDU,i})}{\eta_{PDU,i}} \tag{19}$$

where n is the total number of systems that are active in each of the satellite's simulated modes of operation, $P_{Load,i}$ is the electrical power required by each active system in W, and $\eta_{PDU,i}$ is the efficiency of the relevant electrical power distribution channel.

Complete EPS thermal modeling also requires quantifying the heat dissipated by battery packs of ERMIS-3. In that regard, the heat dissipated by the 18650 Li-ion cells of the two GomSpace NanoPower BP8 battery packs [58] present on ERMIS-3 ($\dot{Q}_{Bat.}$) was estimated using the Joule heating relation as described by Equation (20). Since each battery pack is comprised of eight series-connected 18,650 Li-ion cells, the total pack resistance equals the sum of the individual ohmic cell resistances. The total resistance of each battery pack is then multiplied with the square of the net current running through the cell string to calculate the dissipated heat. To account for cell degradation over the mission's duration, the "Cold" cases utilized baseline resistance values corresponding to new cells, while the "Hot" cases incorporated elevated cell resistance values to simulate increased heat dissipation. Specifically, for brand-new cells, the resistance of each cell was considered to be 0.040 Ω, leading to a total resistance of 0.320 Ω for each battery pack. Similarly, for degraded cells, the resistance of the cells was increased by 50%, leading to 0.060 Ω for each cell and 0.480 Ω for each battery pack. The 50% battery resistance increase considered in these cases corresponds to an End-of-Life battery condition, as reported for similar Li-ion batteries [59]. Additionally, since charge current of the battery is dependent on its charge voltage, which can change depending on the battery charge levels, 22 V was considered for charging during the "Hot" cases and 32 V in the "Cold" cases. Therefore, the charge current of the battery (I_{Charge}) can be calculated using Equation (21). The discharge current

of the battery ($I_{Discharge}$), on the other hand, is always dependent on the operation of the satellite's various systems and is different in each simulated mode of operation.

$$\dot{Q}_{Bat.} = R_{Total} I_{Net}^2 = R_{Total} (I_{Discharge} - I_{Charge})^2 \quad (20)$$

$$I_{Charge} = \frac{\eta_{ACU} P_{Generated}}{V_{Charge}} \quad (21)$$

where I_{Net} is the net current flowing through the Li-ion cells in A, which is equal to the difference between the discharge current ($I_{Discharge}$) and the charge current (I_{Charge}), R_{Total} is the total ohmic resistance of the cells that make up each battery pack in Ω, η_{ACU} is the efficiency of the ACU, $P_{Generated}$ is the electrical power generated by the satellite's solar arrays in W, and V_{Charge} is the battery charge voltage in V.

For thermal control reasons, each NanoPower BP8 battery pack is equipped with a 6 W electrical heating element. In the FE thermal model of ERMIS-3, these heaters are controlled via implicit events triggered by the temperature of the 18,650 Li-ion cells. The control logic follows a hysteresis concept, as the 6 W heat source is activated when the temperature drops below 2 °C and deactivated once it rises above 6 °C. Each battery pack is monitored independently, allowing for autonomous heating element control. Through this procedure, the dynamic heat load of the heaters is factored into the satellite's thermal balance in a realistic manner throughout the simulation. The heating load of the electrical heating elements is denoted in the thermal model of ERMIS-3 as $\dot{Q}_{Heater}$.

Having established the rationale behind the modeling of the EPS operation and the dynamic activation of certain mission-critical components, Figures A1 and A2 of Appendix A.1 provide detailed curves for the relevant variables and values included in Table 6.

Following standard industry practice in the field of spacecraft FE thermal analysis, the geometric model of ERMIS-3 was idealized compared to its detailed CAD model. This simplification reduces computational complexity and consequently, simulation time, while at the same time maintaining a high degree of result accuracy. The external geometry of the idealized model of ERMIS-3 used for the thermal analysis is shown in Figure 7 from different perspectives, while Figure 8 presents detailed renderings of the model's internal subsystems and configuration.

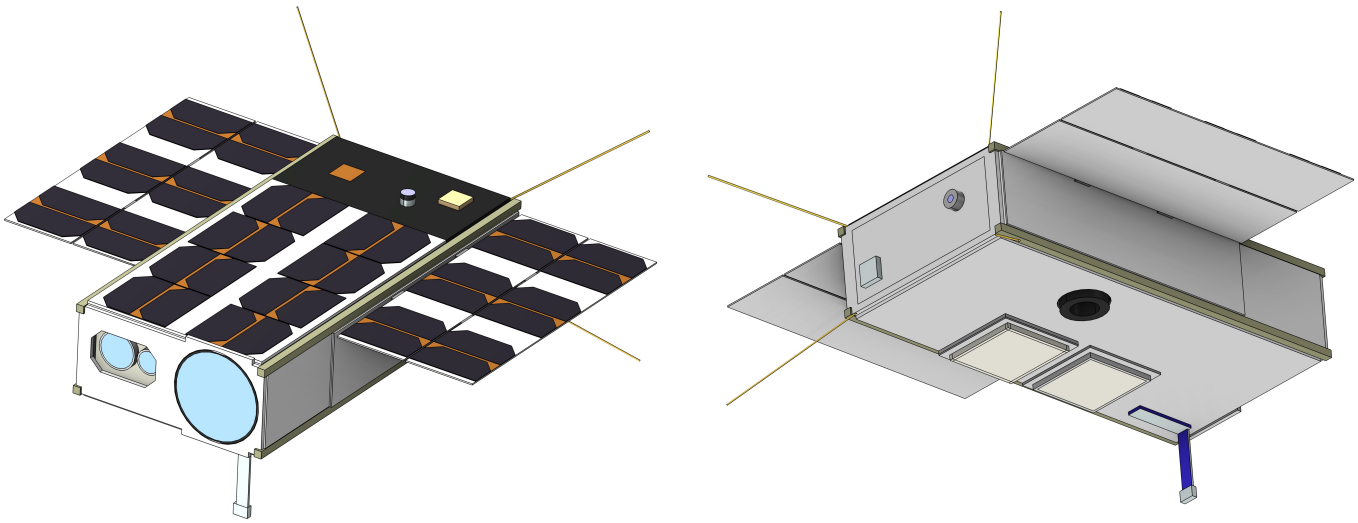

Figure 7. External views of the idealized geometric model of ERMIS-3 used for its thermal analysis.

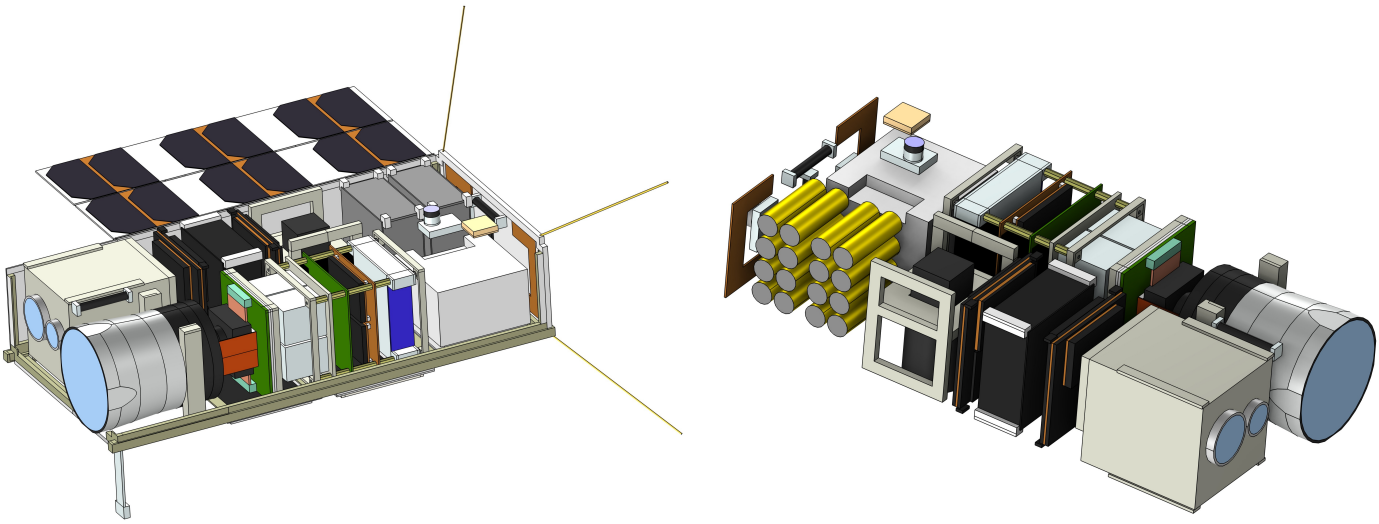

Figure 8. Renderings of the internal configuration of the idealized geometric model of ERMIS-3.

Nevertheless, to model a satellite's thermal behavior accurately, attention should always be paid to the mass of each of its individual subsystem FE models, as well as to the total mass of the satellite's complete FE thermal model. This is because the temperature of each component is directly linked to its thermal inertia, as expressed by Equation (5). Therefore, significant attention was paid in the creation of simplified equivalents for each of the satellite's platform subsystems and payloads that feature the same mass as the value reported for the real components of the satellite, or at worst exhibit a mass deviation that is less than 1% of the actual component mass. The discrepancy between the total 11.191 kg mass calculated by the detailed CAD model and the 11.200 kg mass of the idealized thermal model of ERMIS-3 (excluding the mass of the satellite's harness) was found to be only 0.080%, which is considerably lower than the 1% target set initially, indicating an excellent correlation. Furthermore, since radiative heat transfer is one of the two mechanisms (along with that of heat conduction) of heat transfer inside the satellite and the only mechanism that governs heat transfer between the satellite and its surrounding environment, significant attention was also paid in maintaining the overall shape of all the modeled components of ERMIS-3, despite the significant geometric simplification applied to the geometric representation of the satellite's thermal model.

Finally, the thermal model of ERMIS-3 was discretized into finite elements using the integrated meshing tool of the COMSOL Multiphysics simulation suite. In general, a more refined mesh was utilized in regions of increased thermal interest, such as electronic boards and other subsystem models, compared to less critical regions of the satellite, such as its structural elements. For the discretization of the thermal model of ERMIS-3, a combination of tetrahedral, hexahedral, pyramidal, and prismatic elements was utilized, based primarily on the geometric features and complexity of each individual domain that required meshing, as well as its interfaces and the features of any neighboring domains that are thermally coupled with it. Additionally, to ensure an acceptable balance between the accuracy of the numerical model's results and its computational complexity, a mesh convergence study was performed prior to the final simulation runs. The results of this mesh convergence study and the details of the final mesh are presented in Appendix B together with the results of a radiation resolution convergence study, a temporal resolution analysis, and a thermal energy balance verification check.

5. ERMIS-3 Radiation Analysis Results

This section presents some key results of the radiation analysis simulations for the CubeSat ERMIS-3. The computation of the surface-to-surface radiative loads of the analysis was conducted using the Ray Shooting method, which has been documented to be capable of producing more accurate results compared to Hemi-Cube methods [60]. The results of the radiation analysis are foundational as they form the basis on which the subsequent thermal analysis of the satellite takes place. Additionally, the results of this analysis were also crucial in calculating the electrical power that is generated by the solar arrays of ERMIS-3, which was in turn used to model the thermal behavior of the EPS of the satellite in a dynamic and realistic manner while also providing essential inputs for preliminary electrical power management simulations.

As mentioned previously, the thermal analysis of ERMIS-3 is divided into two "Hot" and two "Cold" cases. Therefore, to account for the hottest possible scenario the satellite may need to operate in, the simulated "Hot" case corresponds to the Winter Solstice (near Perihelion), where the direct solar flux approaches its highest value of 1414 W/m^2 [24], while following the same philosophy, to simulate the coldest possible scenario, the "Cold" case corresponds to the Summer Solstice (near Aphelion), where the solar flux approaches its annual minimum of 1322 W/m^2 [24]. Furthermore, different extreme values of the Earth IR and albedo radiation were also used in each case. More specifically, in the "Hot" cases, an albedo fraction value that is equal to 0.40 [26] and an Earth IR flux of 243 W/m^2 [39] were used, while for the "Cold" cases, an albedo fraction equal to 0.25 [26] and an Earth IR flux of 218 W/m^2 [39] were utilized. In all the simulated cases, the effective temperature of space was set at 2.73 K [61].The orbit that was simulated in COMSOL Multiphysics for all the different cases is a circular SSO with an altitude of 510 km and an inclination of 97.45°, with only the orbit's LTAN changing between the two cases. While the actual final orbit of ERMIS-3 is slightly elliptical (a fact that was expected even at the design and analysis stage of the mission, by review of previous SpaceX launch missions), the 510 km orbit considered in the analysis is a conservative simplification that does not significantly impact the validity of the acquired results.

The complete information about the "Hot" and "Cold" orbital thermal environment cases considered in the radiation analysis and subsequent thermal analysis of ERMIS-3 is summarized in Table 7, along with the different energy conversion efficiency considered for the solar cells in each case. In COMSOL Multiphysics, the radiation spectrum of the analysis was divided into the solar band, which encompasses the part of thermal radiation with wavelengths up to 2500 nm and the ambient band (predominantly Earth IR) which encompasses the part of thermal radiation which has wavelengths greater than 2500 nm.

Visualizations of the two simulated orbits are provided in Figure 9 along with the distribution of the albedo radiation intensity plotted on the surface of the planet for both simulated orbital thermal scenarios. In this figure, the yellow arrows define the direction of the direct solar flux, while the yellow and black segments of the orbital path represent the sunlit and eclipse regions of the orbit, respectively. From the results of the radiation analysis simulations that are presented in Figure 9, it is clearly visible that the albedo radiation reaches its maximum intensity at the subsolar point, something that matches the information reported in [24]. Additionally, as expected, the albedo flux of the "Hot" case reaches noticeably higher values (namely reaching 565.60 W/m^2 at its maximum point) than the albedo flux of the "Cold" case (which reaches 330.50 W/m^2 at its maximum point), in a manner that is proportional to the differences between the albedo fractions and direct solar fluxes that were considered in the two scenarios. From these simulations, the orbital period was calculated at 5689.40 s. The resulting eclipse durations of the two considered orbits are directly governed by their respective β angles. More specifically, for the "Cold"

bounding case (LTAN 13:00:00 at the Summer Solstice), the small β angle of approximately 10.59° places the orbital plane firmly close to the Earth's shadow vector, resulting in an eclipse duration of 2130.50 s. This prolonged shadowing of the satellite minimizes its continuous exposure to the solar flux, driving it toward lower temperatures. On the other hand, the "Hot" bounding case (LTAN 15:00:00 at the Winter Solstice) yields a significantly larger β angle of approximately 44.01°, which tilts the orbital plane further out-of-plane relative to the Sun, thus reducing the eclipse duration to 1843.50 s and resulting in a more prolonged solar exposure that increases on average the thermal loads that are incident to the satellite, leading to higher temperatures.

Table 7. An overview of the parameters used in the two possible extreme orbital thermal environment cases considered in the thermal modeling and analysis of the CubeSat ERMIS-3.

Parameter Definitions	**Simulated Orbital Thermal Case**	
	Cold	**Hot**
Orbital Information		
Altitude (km)	510	510
LTAN (h:min:s)	13:00:00	15:00:00
Inclination (°)	97.45	97.45
Thermal Conditions		
Direct Solar Flux (W/m^2)	1322	1414
Albedo Fraction	0.25	0.40
Earth IR Flux (W/m^2)	218	243
Space Temperature (K)	2.73	2.73
Satellite-Related Parameters		
Solar Cell Efficiency	26.50%	25.50%

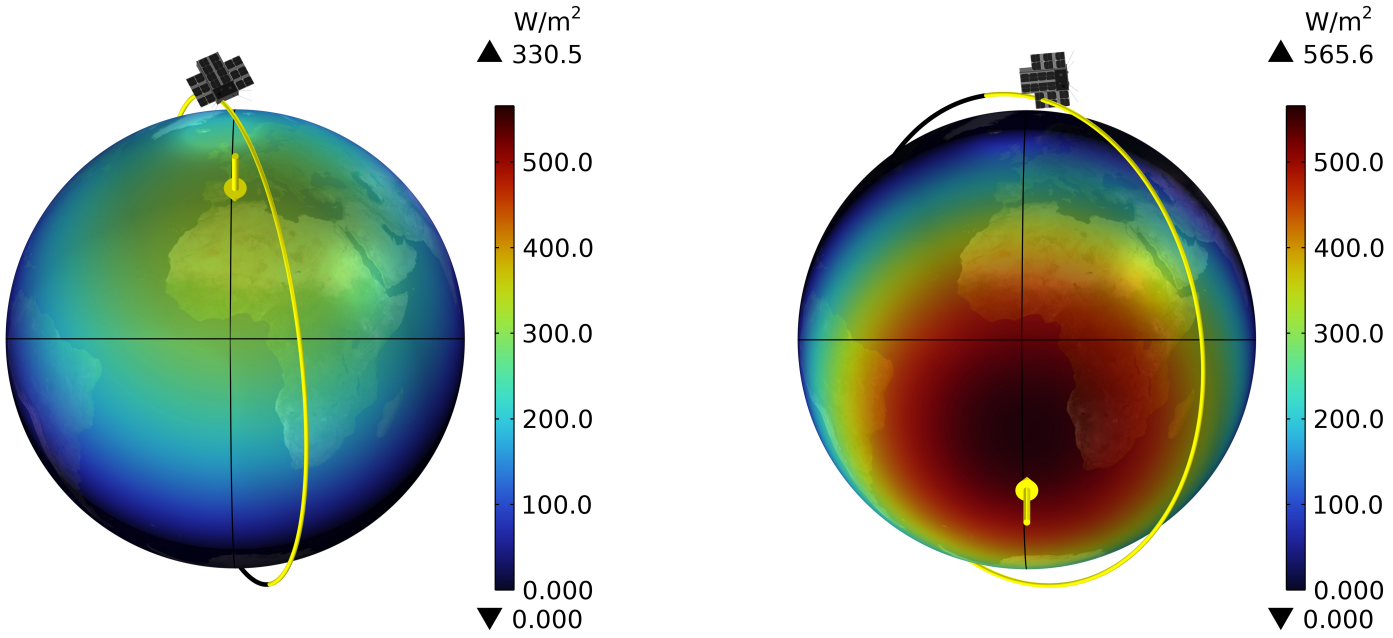

(**a**) (**b**)

Figure 9. A visualization of the two simulated orbits of ERMIS-3, along with the calculated albedo flux. (**a**) In the simulated "Cold" case (LTAN 13:00:00, solar flux equal to 1322 W/m^2, and albedo fraction equal to 0.25). (**b**) In the simulated "Hot" case (LTAN 15:00:00, solar flux equal to 1414 W/m^2, and albedo fraction equal to 0.40).

Figure 10 presents the radiative thermal power from external heat sources (the Sun and the Earth) that is incident to the surfaces of ERMIS-3 during Sun-tracking operations, for both the "Cold" and "Hot" simulated orbital thermal condition scenarios. More specifically, Figure 10a presents the incident solar band and ambient band radiative power along with the total incident radiative power (the sum of both bands) during the "Cold" orbital thermal conditions case. Following the same philosophy, Figure 10b presents the same data for the "Hot" orbital thermal conditions case. In both cases, the simulation begins with the satellite located at the equator (0° latitude) and includes three complete orbits. Accordingly, Table 8 provides a comparison between the orbit-averaged values of the solar and ambient band radiative power, along with the orbit-averaged value of the total radiative power that is incident on the surfaces of ERMIS-3 while the satellite operates in Sun-tracking mode, during both of the extreme "Hot" and "Cold" scenarios. The results indicate that as a result of the higher solar flux, Earth IR flux, and albedo factor, as well as the shorter eclipse duration of the orbit considered for the "Hot" scenario, the total orbit-averaged irradiation of the satellite's surfaces is 13.39% higher compared to the orbit-averaged value calculated for the "Cold" simulated scenario.

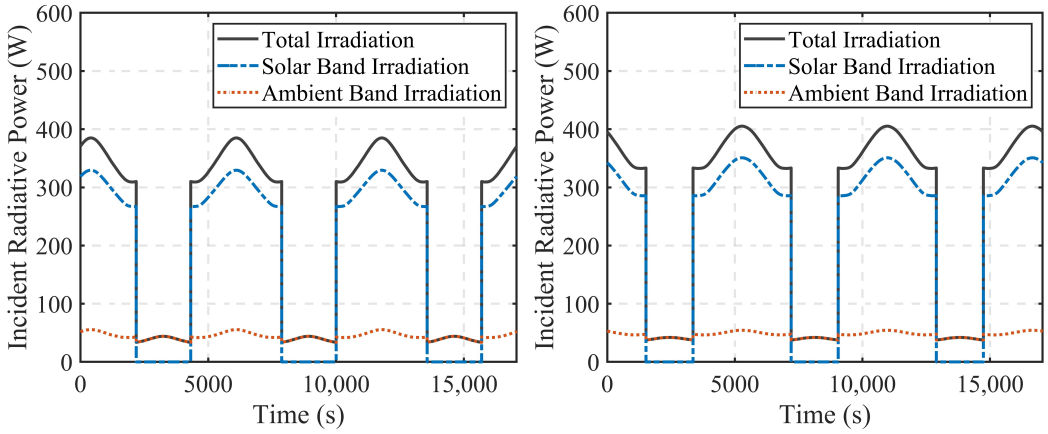

Figure 10. A visualization of the solar band, ambient band, and the total radiative power from external sources that is incident to the surfaces of the CubeSat ERMIS-3. (**a**) While the satellite is in Sun-tracking mode during the "Cold" case. (**b**) While the satellite is in Sun-tracking mode during the "Hot" case.

Table 8. The orbit-averaged values of the solar band, ambient band, and the total radiative power from external heat sources that is incident to the surfaces of the ERMIS-3 during the "Cold" and "Hot" simulated cases, for Sun-tracking attitude.

Radiation Spectral Band	Orbit-Averaged Incident Radiation (W)	
	Cold Case	Hot Case
Solar Band	184.65	212.85
Ambient Band	44.07	46.49
Total Irradiation	228.72	259.34

Finally, as it represents a direct result of the solar band radiation (both direct solar and albedo) that is incident to the satellite's solar cells, the electrical power generated by ERMIS-3 while in Sun-tracking mode of operation is presented in Figure 11, over three complete orbits. The presented results incorporate the specific energy conversion efficiencies defined for the "Cold" and "Hot" cases respectively. The acquired results indicate that the instantaneous electrical power generation during the "Hot" scenario is higher

than that of the "Cold" scenario, despite the lower energy conversion efficiency of 25.50% used for the "Hot" orbit scenario. This increased instantaneous generated electrical power, when also coupled with the shorter eclipse duration of the "Hot" orbit which has an LTAN 15:00:00 compared to the "Cold" orbit, which has an LTAN 13:00:00 leads to a noticeably higher orbit-averaged electrical power generation value during the "Hot" scenario. These electrical power generation values calculated through these simulations served as the basis for the thermal modeling of the satellite's EPS, in accordance with the procedure described in Section 4. Additionally, they were also used for a series of preliminary electrical power management simulations.

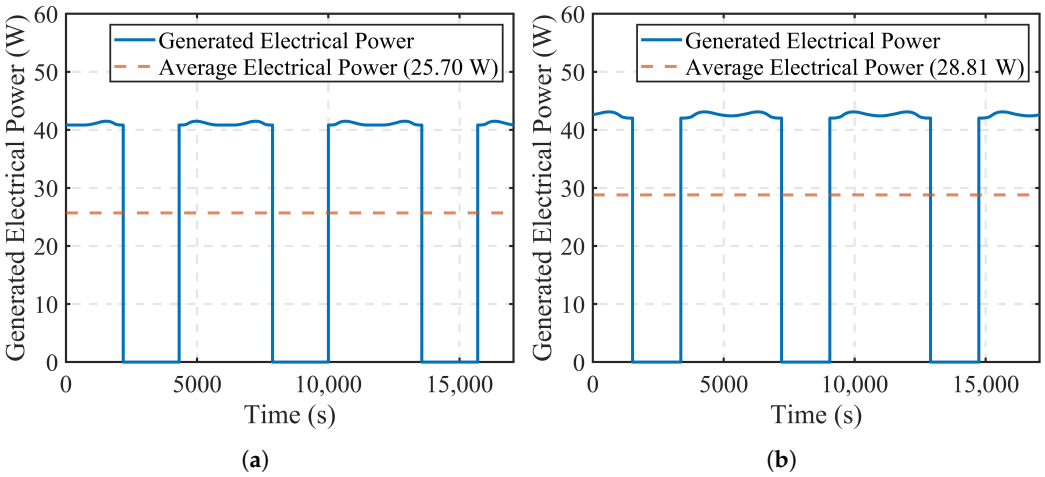

Figure 11. The electrical power that is generated by the solar arrays of ERMIS-3 for a period of three complete orbits while the satellite operates in Sun-tracking mode. (**a**) During "Cold" orbital thermal conditions. (**b**) During "Hot" orbital thermal conditions.

6. ERMIS-3 Thermal Analysis Results

This section presents the temperature results for the individual platform subsystems and payloads of the CubeSat ERMIS-3 across the four simulated operating scenarios, as determined by the FE thermal model of the satellite. Figure 12 provides an overview of the temperature distribution at a specific instant in the sunlit portion of the orbit during Sun-tracking operations, close to the time-point where the average temperature of ERMIS-3 approaches its maximum, for both "Cold" and "Hot" orbital conditions. Conversely, Figure 13 presents the temperature distribution of ERMIS-3 in the eclipse portion of the orbit at a specific time-point when the satellite's average temperature approaches its minimum, for both "Cold" and "Hot" orbital conditions again.

Based on these results, one may observe that when ERMIS-3 is exposed to the direct solar flux, the components that reach the highest temperatures are its deployable solar panels and the monopole rods of its deployable UHF antenna. This is a result of both the high solar absorptivity of the solar cell surfaces, as well as the fact that the hinge mechanisms of these deployable components isolate them from the rest of the satellite due to their low thermal conductance. Conversely, the internal components of ERMIS-3 that are the hottest in these conditions are the NanoPower P80 EPS and the NanoDock DMC-3 motherboard which contains the NanoMind A3200 OBC, the NanoCom AX100 UHF radio transceiver, and the OEM719 GNSS receiver modules. Furthermore, the considered environmental conditions (direct solar flux, albedo, Earth IR, and LTAN) also have a significant impact on the temperatures of the satellite, with the maximum temperature of ERMIS-3 during the "Hot" orbit case being 63.50 °C, a value that is 9.10 °C higher than the one calculated during the "Cold" orbit case. Regarding the minimum calculated

temperatures of ERMIS-3 during the same period, these stand at 0.52 °C for the "Hot" orbit case and at −7.82 °C for the "Cold" one.

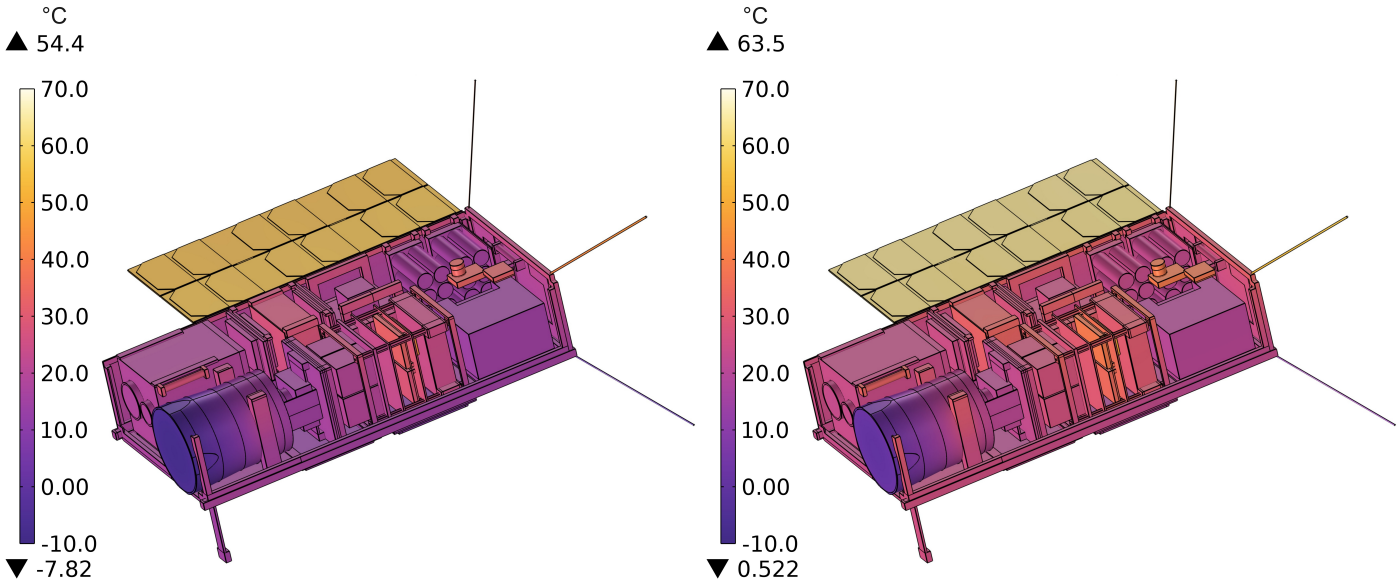

(**a**) (**b**)

Figure 12. The temperature distribution of ERMIS-3 while in the sunlit portion of the orbit and in Sun-tracking mode of operation. (**a**) During the "Cold" orbital thermal conditions scenario. (**b**) During the "Hot" orbital thermal conditions scenario.

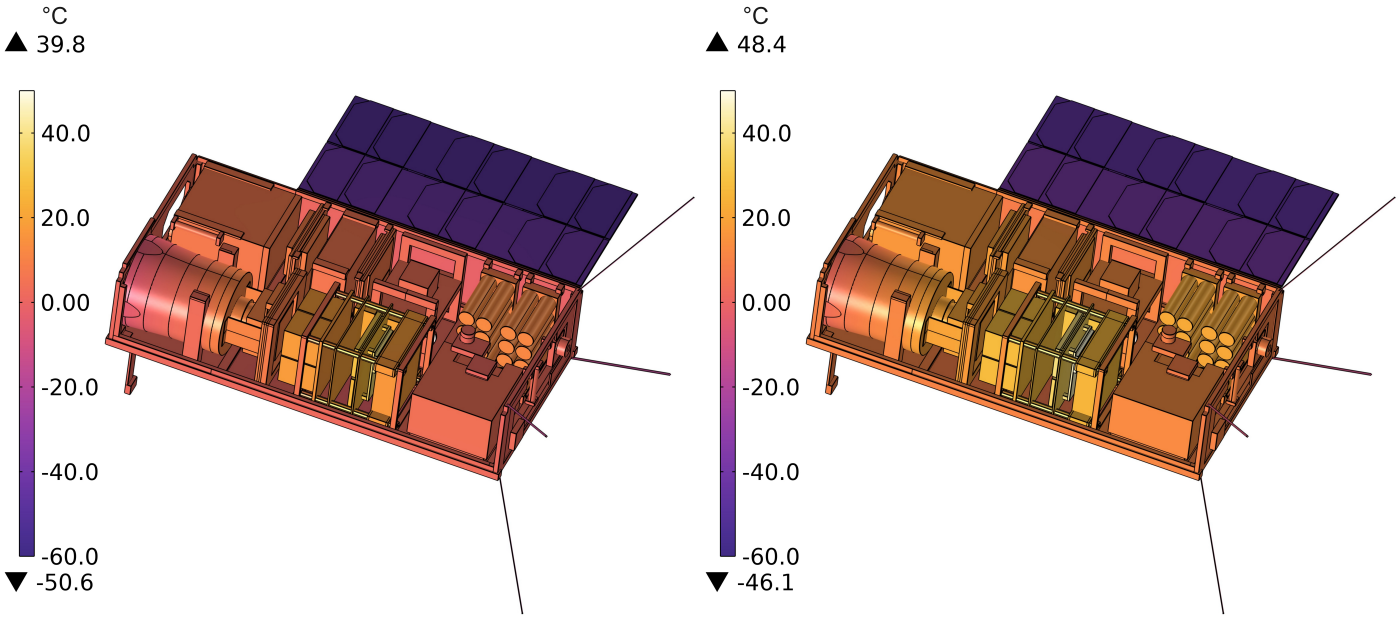

(**a**) (**b**)

Figure 13. The temperature distribution of the CubeSat ERMIS-3 while in the eclipse portion of the orbit. (**a**) During the "Cold" orbital thermal conditions scenario. (**b**) During the "Hot" orbital thermal conditions scenario.

When in the shadow of the eclipse, the hottest region of the satellite is its PC/104 stack, and more specifically the NanoDock DMC-3 and its three daughterboards, which are constantly operational and dissipate a notable amount of heat. The Li-ion cells of the NanoPower BP8 battery packs are also maintained at relatively high temperatures. Due to

their thermal isolation from the rest of the satellite, the components that reach the lowest temperatures during the eclipse are the UHF antenna monopoles and the deployable solar panels, with the high IR emissivity of the solar cells and the clear anodized aluminum panels of the latter also contributing heavily to the rapid cooling effect, due to high radiative heat loss. The environmental factors remain significant in the eclipse portion of the orbit, with the maximum calculated temperature of the satellite in the "Hot" orbit case standing at 48.40 °C, a value that is considerably higher than that of the "Cold" orbit case, which is equal to 39.80 °C. Similarly, during the eclipse portion of the "Cold" orbit case, ERMIS-3 reaches a minimum temperature of −50.60 °C, a value that is 4.50 °C lower than the −46.10 °C minimum temperature calculated for the "Hot" orbit case. Notably, in all cases presented in Figures 12 and 13, the exposed glass end of the HyperScape 100 imager remains the coldest among the internal components of ERMIS-3 due to its high IR emissivity.

Figure 14 presents a comparison of the calculated average temperature for the entire ERMIS-3 FE model over a period of 11 complete orbits around the Earth, covering the four simulated combinations of operating modes and orbital thermal conditions. When comparing the average temperatures of the two "Cold" case scenarios it is visible that during the Sun-tracking mode the orbit-averaged temperature of the satellite is 13.48 °C, a value that is considerably higher than that of the safe mode, which is equal to 0.25 °C, representing a difference of 13.23 °C. Furthermore, the fluctuation of the Sun-tracking mode case's calculated average temperature is also more pronounced at a ΔT of 16.50 °C between the maximum and minimum calculated average temperature, compared to a ΔT of 14.14 °C for the average temperature calculated during the safe mode case simulation. These results are physically consistent, as during the Sun-tracking mode, the satellite's external surface, which contains its solar arrays, has a stable view of the Sun, leading to a greater irradiation of its surfaces, and therefore, to higher temperatures before the satellite starts cooling again as it enters the eclipse portion of the orbit.

Moreover, when comparing the Sun-tracking fractions of the two "Hot" cases with that of the "Cold" Sun-tracking case (see Figure 14 again), a significant difference can be observed in the calculated average temperature of ERMIS-3. More specifically, when in Sun-tracking mode under "Hot" orbital conditions, ERMIS-3 is calculated to have an orbit-averaged temperature of 22.41 °C, a temperature that is 8.93 °C higher than the orbit-averaged temperature calculated for Sun-tracking operations during the "Cold" orbit case. This result can be attributed to the higher direct solar flux, albedo, and Earth IR conditions used in the "Hot" case simulations, as well as to the shorter eclipse duration of the orbit considered in these cases. Lastly, the operation of the payloads of ERMIS-3 over a period that covers two specific orbits leads to a pronounced rise in the satellite's calculated average temperature, with the case of hyperspectral imaging under "Hot" orbital conditions leading to an orbit-averaged temperature of 24.39 °C during the course of the two orbits of interest, while the case of laser-optical communications leads to an orbit-averaged temperature of 25.54 °C over the two orbits of interest. The observation of higher average temperatures during the laser-optical communications mode of operation is reasonable and expected due to the higher heat dissipation of ERMIS-3 during this mode of operation. In both of the "Hot" cases, it is observed that the average temperature of the satellite returns to its original state after the passing of three orbits.

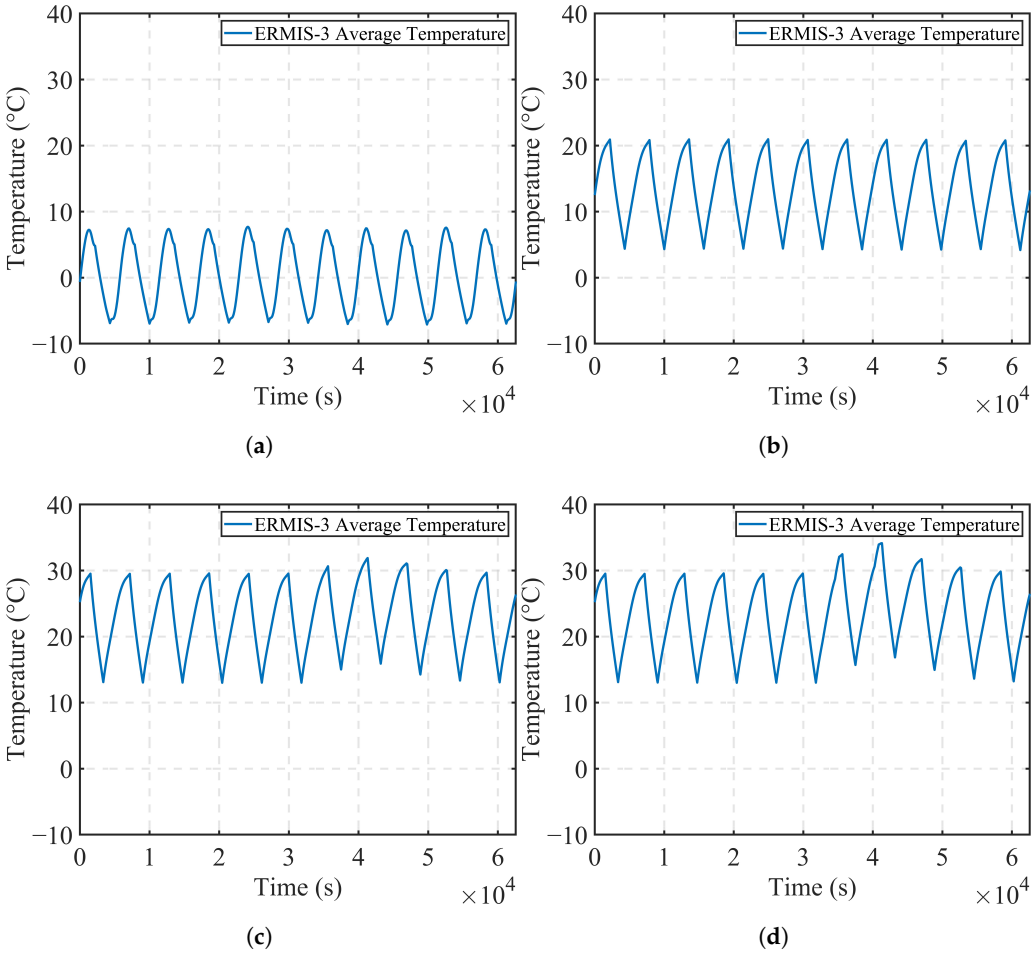

Figure 14. The time-history of the average temperatures of the CubeSat ERMIS-3 for the four simulated combinations of operating modes and orbital thermal conditions over a period of 11 complete orbits. (**a**) For the safe mode and "Cold" orbital thermal conditions scenario. (**b**) For the Sun-tracking mode and "Cold" orbital thermal conditions scenario. (**c**) For the hyperspectral imaging mode and "Hot" orbital thermal conditions scenario. (**d**) For the laser-optical communications link mode and "Hot" orbital thermal conditions scenario.

Figure 15a presents the evolution of the average temperatures of the payload components ERMIS-3 is equipped with, in the case where the satellite is performing nominal Sun-tracking operations under the conditions of a "Hot" orbit and during the 5th and 6th simulated orbits, it switches into hyperspectral imaging mode. Similarly, Figure 15b presents the average temperature evolution of the satellite's payload components in the case where the satellite is performing nominal Sun-tracking operations under the conditions of a "Hot" orbit and during the 5th and 6th orbits again, it switches into laser-optical communications mode of operation. In both cases, after the execution of the payload operations during these two aforementioned orbits, the satellite resumes operating in Sun-tracking mode.

In the case of hyperspectral imaging, a sharp increase can be observed in the average temperatures of the PDPU and the HyperScape100 imager, with the rise of the PDPU being more pronounced, reaching at its maximum point 40.91 °C, an average temperature that is 9.04 °C higher than the maximum value observed during the Sun-tracking sections of the simulation. The average temperature of the HyperScape100 imager during the same period reaches a maximum value of 25.23 °C, a temperature that is 6.53 °C higher than its maximum during the Sun-tracking portion of the simulation. This is a reasonable

result as the ratio of the generated heat to the mass of the PDPU is much higher than that of the hyperspectral imager. The average temperatures of the two ATLAS laser-optical communication assemblies also rise slightly in spite of these components not being active during hyperspectral imaging operations. This is a result of the significant rise in the overall heat dissipation of the entire satellite during imaging operations. Similarly, during the laser-optical communications mode of operation there is a pronounced increase in the average temperature of the PDPU and the ATLAS FSO and ATLAS Amplifier assemblies, all of which are active during this mode, with their average temperatures reaching maximum values of 42.50 °C, 33.84 °C, and 35.04 °C respectively during their operation, which are considerably higher than the highest average temperatures calculated for these components during the Sun-tracking portion of the simulation, by 10.66 °C, 5.09 °C, and 11.64 °C respectively. The non-operational HyperScape100 imager is also heated slightly during the laser-optical communications mode due to its proximity to the other three operational payload components. In both cases, after payload operations end, the average temperatures of the satellite's payloads progressively drop and return to their original states over the next three orbits.

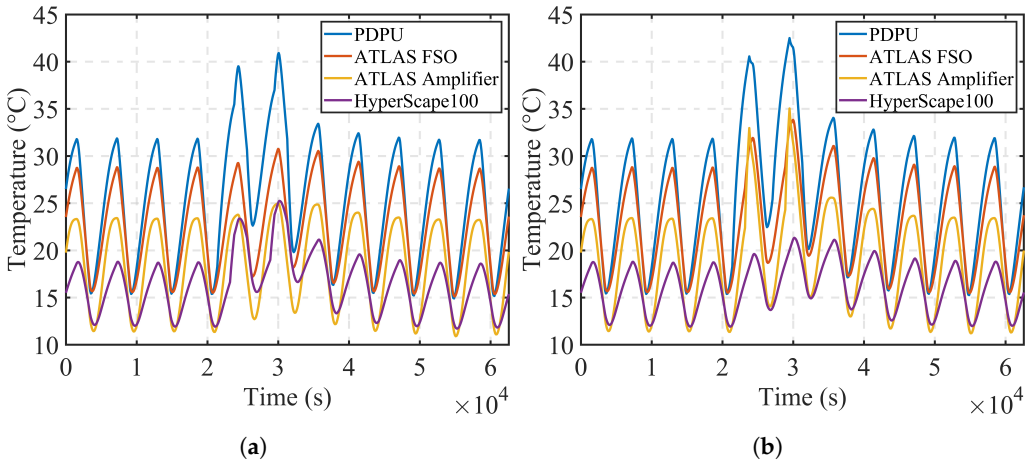

Figure 15. The time-history of the average temperatures of the payloads of ERMIS-3 over a period of 11 orbits during a "Hot" orbit case. (**a**) While in Sun-tracking and hyperspectral imaging modes under "Hot" orbital thermal conditions. (**b**) While in Sun-tracking and laser-optical space-to-ground data transmission modes under "Hot" orbital thermal conditions.

As clearly demonstrated by all the previous results, different subsystems of the satellite can exhibit different temperatures compared to each other at the same time. Furthermore, the temperatures of all the components of the satellite can fluctuate heavily with sunlight/eclipse alternations and component operating cycles (activation/deactivation). Therefore, to evaluate whether any of the component allowable temperature limits are violated, the maximum and minimum temperatures calculated through the FE simulation for each component must be overlaid and compared with the defined allowable limits (operational and non-operational) in a comprehensive manner. Here, it should also be noted that during the thermal modeling and analysis of a satellite, there can always be deviations and inaccuracies regarding the thermal and optical properties utilized in the model compared to those of the actual flight hardware, as well as a considerable degree of uncertainty with regard to the considered thermal contact conductances. Furthermore, the idealization of the FE model's geometry introduces another source of modeling errors and by extension, final result uncertainty. Moreover, as described by [62–64], the exposure of spacecraft or satellite materials and thermal control coatings to the space environment can progressively alter their optical properties and affect the vehicle's thermal behavior.

To account for these modeling inaccuracies and uncertainties, an uncertainty margin was applied to the maximum and minimum calculated temperature value of each component (e.g., the maximum and minimum temperatures calculated by the FE simulation model) as per [65], leading to a wider and more conservative temperature range, which is defined as the predicted temperature range and is the one that is eventually compared to the component allowable temperature limits (see Figure 16). For all the simulated thermal cases of ERMIS-3, the temperature margin was set at 10 °C. This 10 °C uncertainty margin served as the baseline margin maintained throughout the project's design reviews and technical notes presented to ESA and is aligned with relevant information on CubeSat thermal margins reported by other sources, such as [66–68]. Moreover, as demonstrated by the results presented in Appendix A.2, this 10 °C temperature margin can reliably cover the uncertainty that accompanies the modeling of the satellite's thermal contacts.

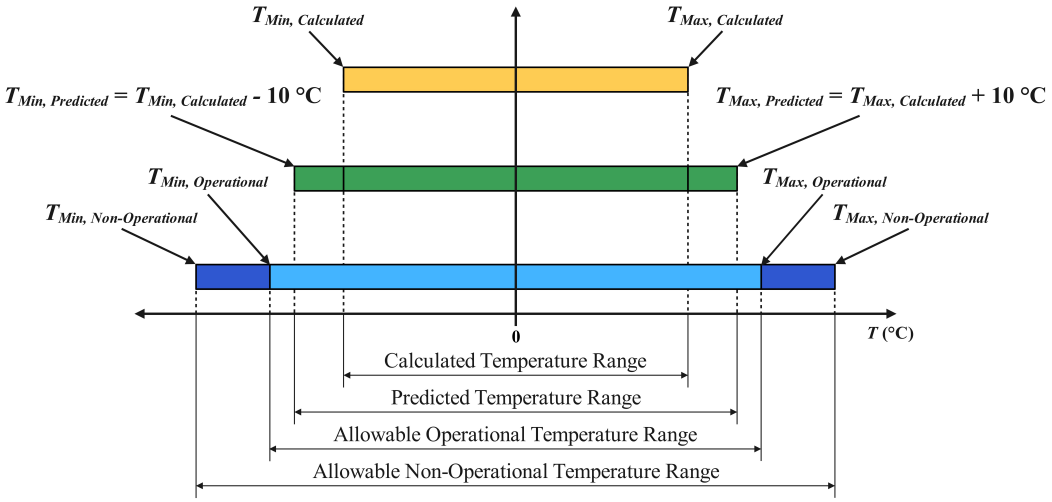

Figure 16. A high-level overview of the procedure followed for the calculation of the predicted temperature range and the comparison with the allowable temperature limits of the individual platform subsystems and payload components of ERMIS-3.

Based on the margin philosophy presented in Figure 16, the following figures feature a series of bar charts that visualize the predicted temperature ranges of each component of ERMIS-3, compared to the allowable operational and non-operational temperature limits of each component. The only exception/adjustment to this rule, is the minimum predicted temperature of the satellite's 18,650 Li-ion cells, where the 2 °C temperature represents a hard limit below which the electrical heating elements of the battery packs are set to be activated, and the temperature of the cells will immediately start rising. Therefore, in these two components, if the minimum predicted temperature is found to be less than 2 °C, the minimum predicted temperature will then be assumed to be equal to 2 °C. In that regard, Figure 17 presents the predicted temperature range of each OBC, GNSS, TT&C, and COMM component of ERMIS-3 compared to the component allowable temperature limits (operational and non-operational) as defined by their manufacturers. Similarly, the same comparison for the ADCS components of ERMIS-3 is provided in Figure 18, for the EPS components in Figure 19, while Figure 20 is dedicated to the four individual mission-enabling payloads of the satellite. In all these figures the allowable operational temperature range of the components is highlighted in cyan color, while the allowable non-operational temperature range is highlighted in dark blue color. For the component predicted temperature range, green is used to symbolize that the component of interest is operational (activated) during the simulation, whereas in cases where the component is non-operational (deactivated), red is used instead.

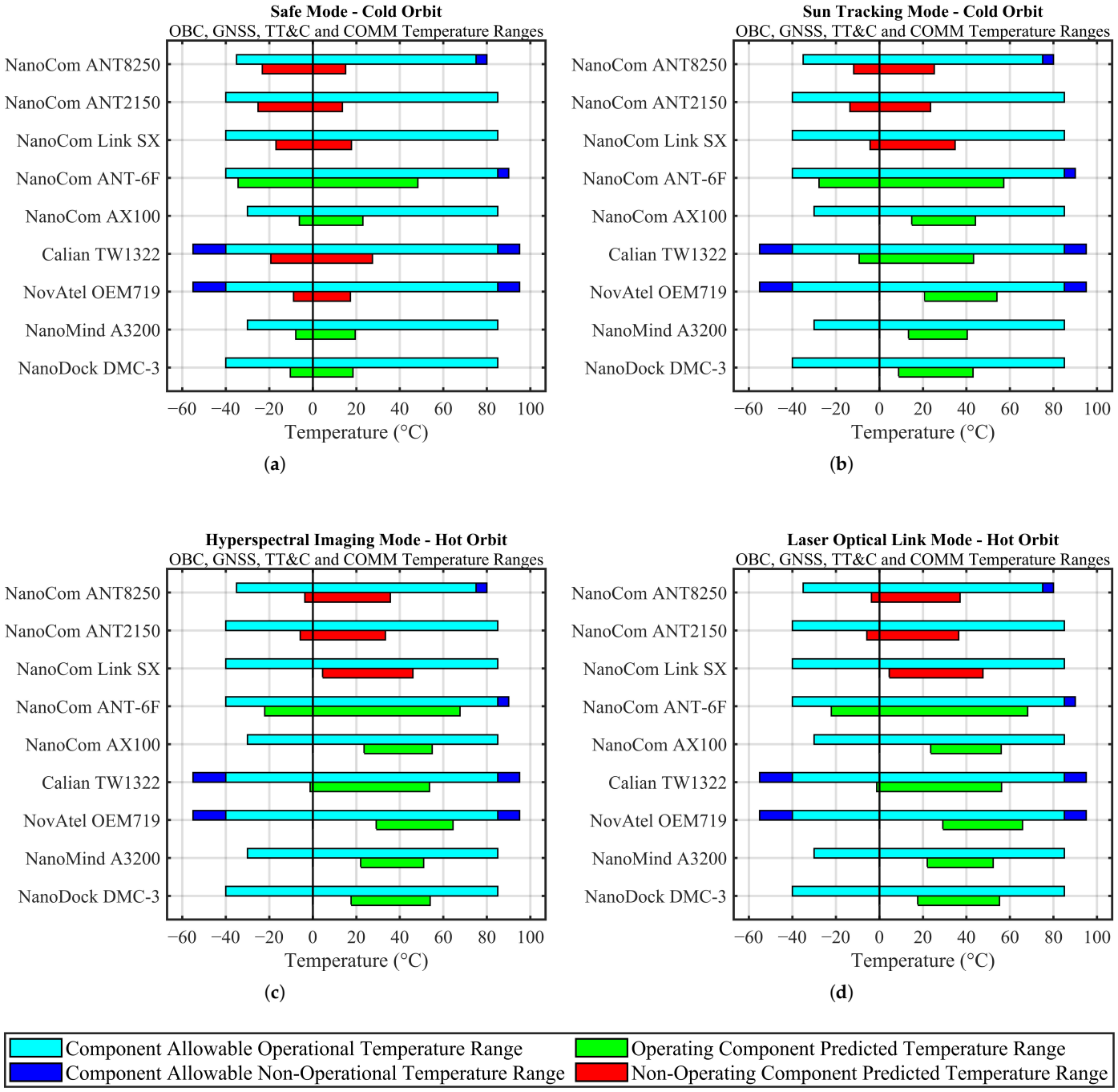

Figure 17. The predicted temperature ranges of the OBC, GNSS, TT&C, and COMM components of ERMIS-3 compared to their allowable temperature limits. (**a**) While in safe mode during a "Cold" orbital thermal scenario. (**b**) While in Sun-tracking mode during a "Cold" orbital thermal scenario. (**c**) While in hyperspectral imaging mode during a "Hot" orbital thermal scenario. (**d**) While in laser-optical communications mode during a "Hot" orbital thermal scenario.

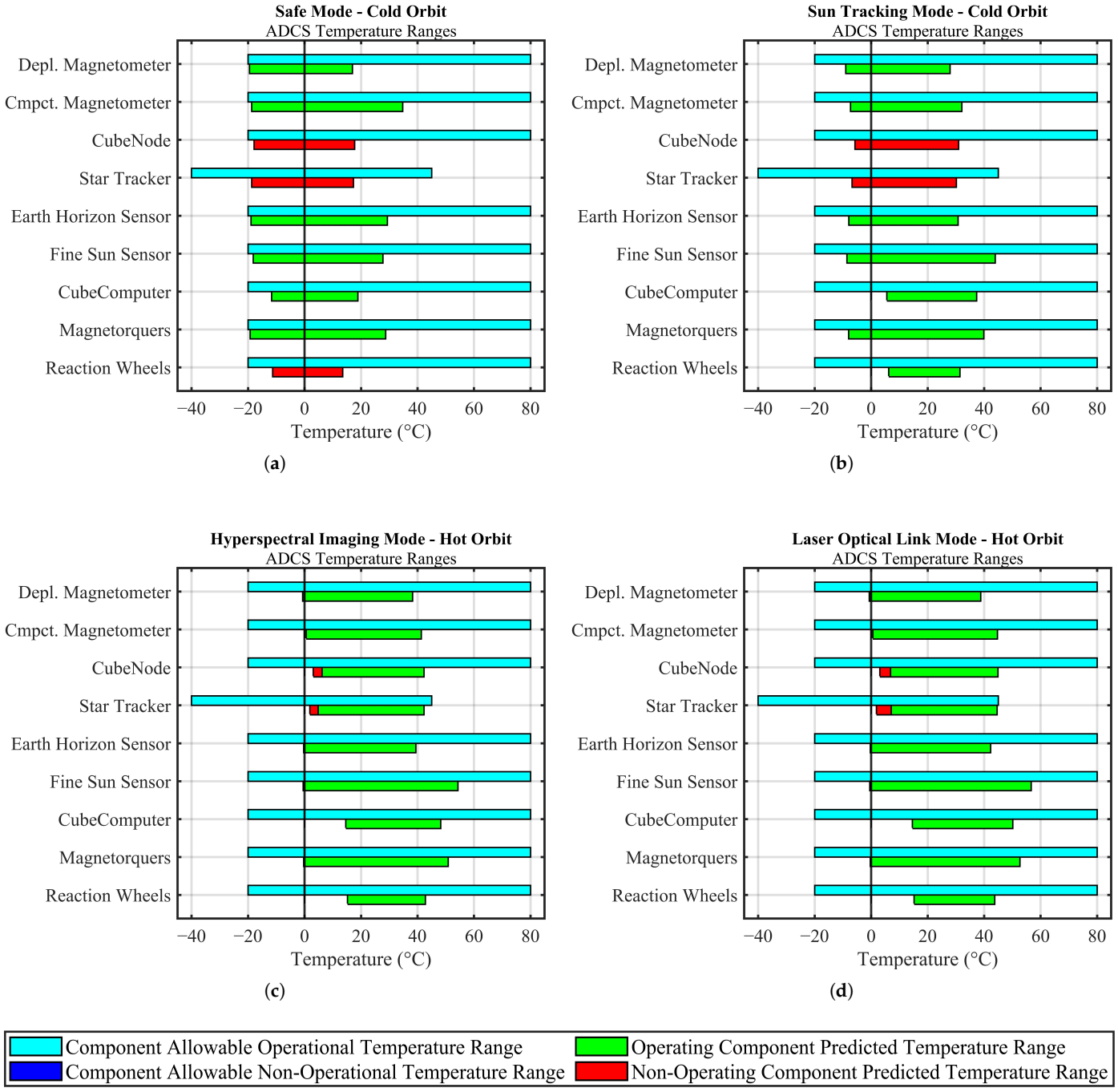

Figure 18. The predicted temperature ranges of the ADCS components of ERMIS-3 compared to their allowable temperature limits. (**a**) While in safe mode during a "Cold" orbital thermal scenario. (**b**) While in Sun-tracking mode during a "Cold" orbital thermal scenario. (**c**) While in hyperspectral imaging mode during a "Hot" orbital thermal scenario. (**d**) While in laser-optical communications mode during a "Hot" orbital thermal scenario.

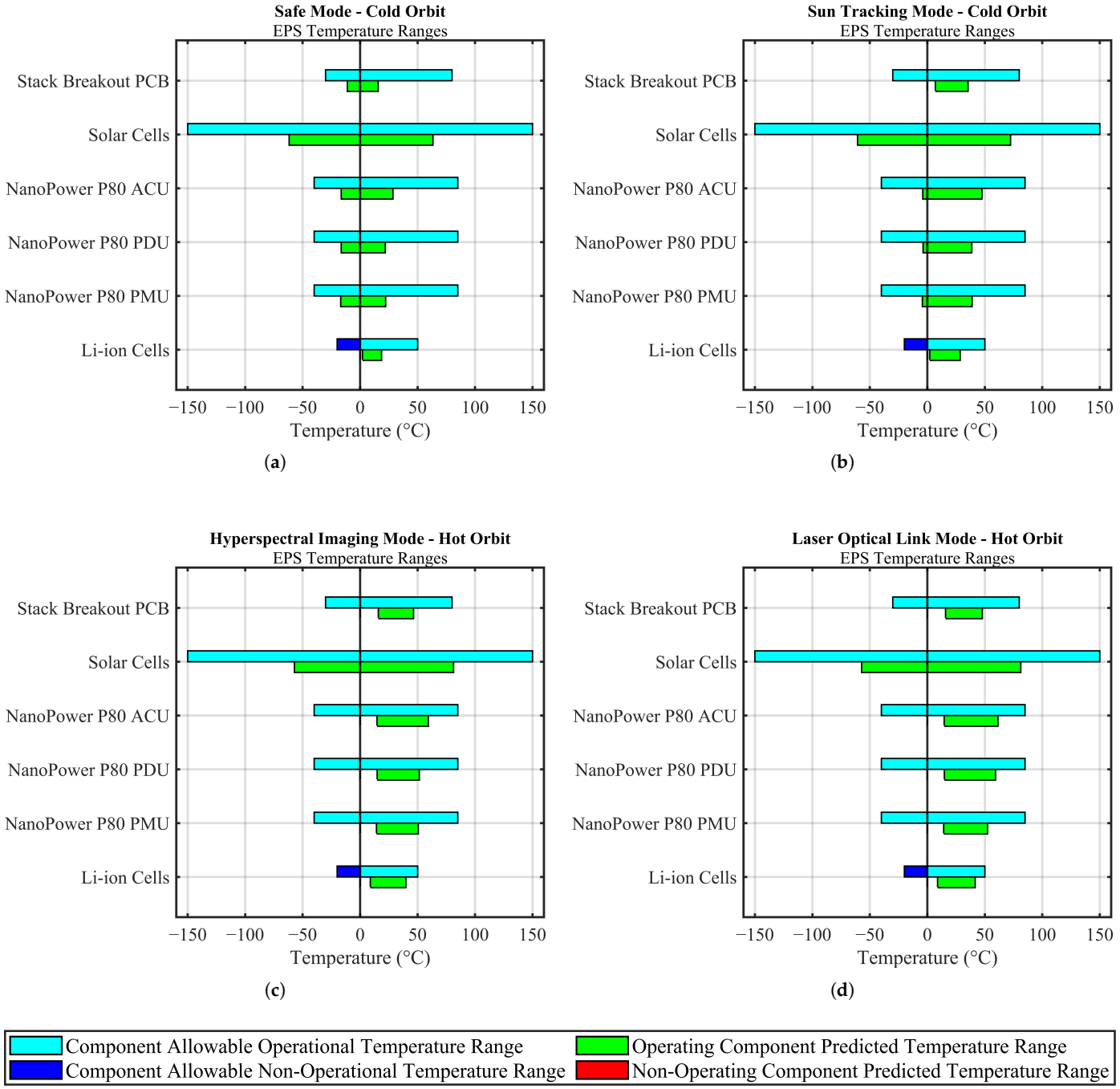

Figure 19. The predicted temperature ranges of the EPS components of ERMIS-3 compared to their allowable temperature limits. (**a**) While in safe mode during a "Cold" orbital thermal scenario. (**b**) While in Sun-tracking mode during a "Cold" orbital thermal scenario. (**c**) While in hyperspectral imaging mode during a "Hot" orbital thermal scenario. (**d**) While in laser-optical communications mode during a "Hot" orbital thermal scenario.

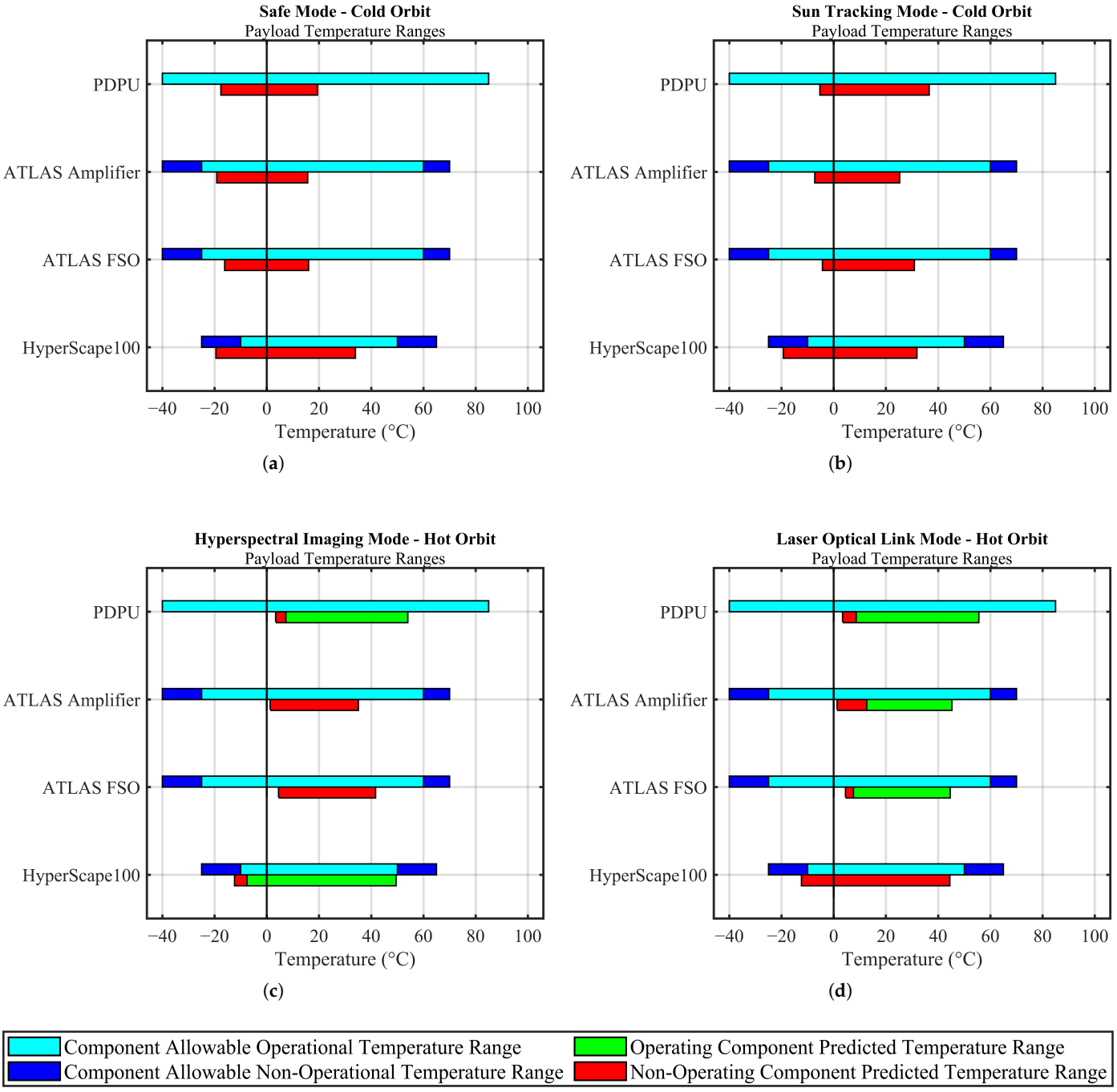

Figure 20. The predicted temperature ranges of the payload components of ERMIS-3 compared to their allowable temperature limits. (**a**) While in safe mode during a "Cold" orbital thermal scenario. (**b**) While in Sun-tracking mode during a "Cold" orbital thermal scenario. (**c**) While in hyperspectral imaging mode during a "Hot" orbital thermal scenario. (**d**) While in laser-optical communications mode during a "Hot" orbital thermal scenario.

The results illustrated in the previous figures are also summarized in a more comprehensive manner in Tables A5 and A6 of Appendix C.

The results of the thermal analysis of ERMIS-3 also provided our team with an estimation of the operating cycles of the electrical heating elements that are integrated into the two NanoPower BP8 battery packs containing the 18,650 Li-ion cells, information which was crucial in estimating the satellite's electrical energy balance during its operation, while also acting as an indicator of the thermal design's soundness, as a prolonged heater operation

result would indicate that revisions should be performed on the thermal design of ERMIS-3. During these simulations, it was found that the heating elements needed to operate only in the scenario that combines the coldest possible orbital thermal conditions with the satellite operating in safe mode. More specifically, the duty cycle for the two 6 W electrical heating elements was calculated at 18.20% and 18.21%, with Figure 21 presenting the detailed electrical heating element operating cycles as calculated by the FE thermal analysis, for both NanoPower BP8 battery packs and for all four simulated scenarios. This result can mainly be attributed to the selection of black anodization (MIL-A-8625 Rev. F Type II Class 2) for the +Y side aluminum panel that covers the batteries, which during nominal Sun-tracking operations absorbs a considerable amount of solar band radiation, due to the black anodization's high solar absorptivity, which in turn helps maintain the Li-ion cells within their nominal operating limits without the need of heating element activation. At the same time, as indicated by the temperature results of all the other simulated cases, the cells are still far from their maximum allowable temperature limits of 50 °C during the simulations that combine the hottest possible orbital conditions with the hottest operational modes of the satellite, with a considerable margin of safety still present. As a result, no risk of battery overheating was identified either.

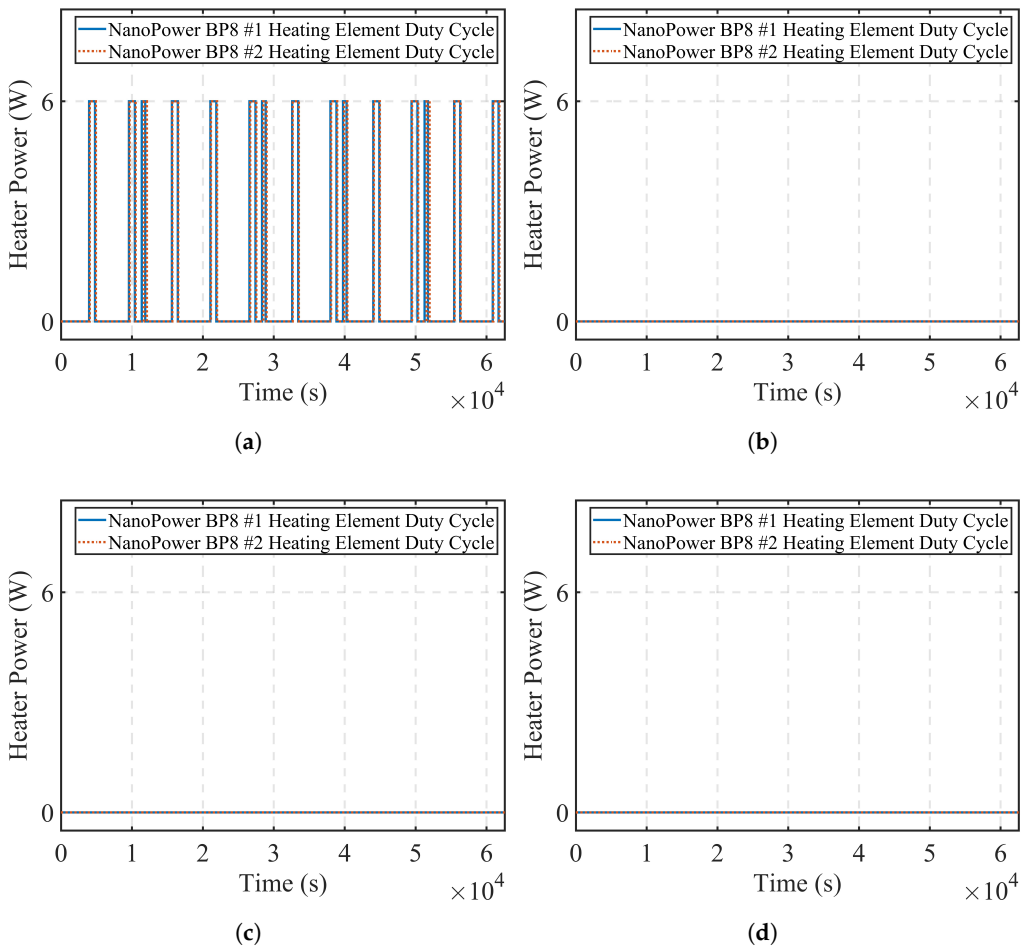

Figure 21. The operating duty cycle of the NanoPower BP8 battery pack 6 W electrical heating elements as calculated by the FE thermal model of ERMIS-3. (**a**) During the safe mode and "Cold" orbital thermal condition case. (**b**) During the Sun-tracking mode and "Cold" orbital thermal condition case. (**c**) During the hyperspectral imaging mode and "Hot" orbital thermal condition case. (**d**) During the laser-optical communications mode and "Hot" orbital thermal condition case.

Overall, the presented results of the simulated cases indicate that ERMIS-3 can survive and operate effectively under all possible thermal conditions that it may need to face in its designated SSO. Furthermore, based on the subsystem predicted temperatures it is also clear that even those scenarios that combine the hottest possible conditions with the hottest possible operational modes, as well as the scenarios that combine the coldest possible conditions with the coldest possible operational modes, are still viable, even with the 10 °C temperature uncertainty margin that was considered in all the calculated subsystem temperatures, as no platform or payload component of ERMIS-3 was found to violate its allowable temperature limits.

Due to the drag of residual atmosphere, the orbital altitude of ERMIS-3 will not remain constant during its mission, but it will progressively decay, until the satellite deorbits and reenters the Earth's atmosphere. Therefore, to evaluate the effect of orbital altitude on the acquired thermal results, two simulations corresponding to Sun-tracking mode under "Hot" orbital thermal conditions were run, with orbital altitudes of 510 km (mission orbit) and 400 km, respectively. The comparison presented in Figure 22 demonstrates that an altitude change of 110 km has a negligible impact on the maximum and minimum values of the average temperature of ERMIS-3, with the difference between the overall mean (time-averaged) temperatures of the two cases not surpassing 0.1 °C. The only significant difference between the two cases is a noticeable phase difference, which is reasonable due to the shorter period of the 400 km orbit. Therefore, the conclusions extracted for the initial orbit can be considered to remain valid and applicable for the entire mission of ERMIS-3.

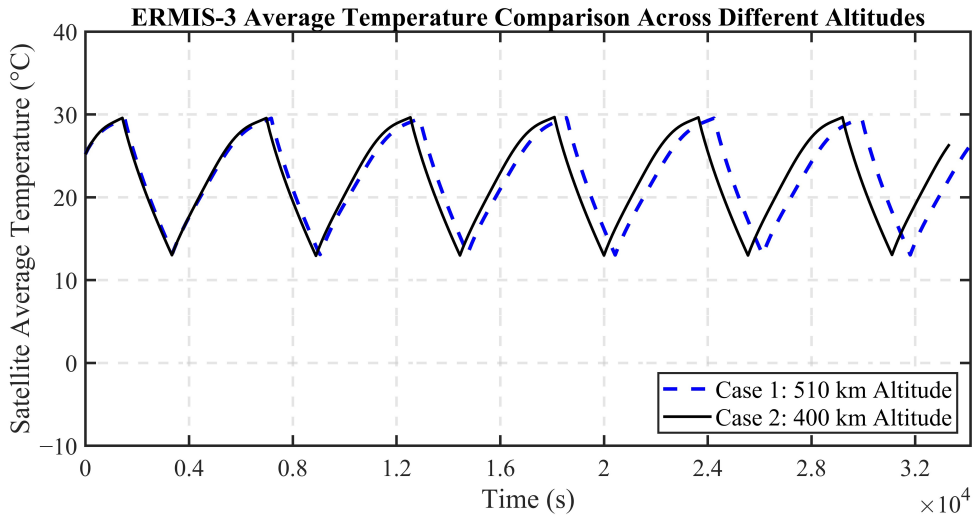

Figure 22. A comparison between the evolution of the average temperature of ERMIS-3 for Sun-tracking operations under "Hot" orbital thermal conditions, for two different altitude cases.

7. Correlation of the Thermal Model with In-Orbit Temperature Measurements

A photograph of the fully assembled and integrated ERMIS-3 in its deployed configuration is presented in Figure 23. This photograph was captured in the cleanroom facility of the NKUA Department of Aerospace Science and Technology, located at the Evripos Campus, Psachna, Evia, Greece. After the conclusion of the assembly and integration phase, the CubeSat ERMIS-3 was transported to the European Space Research and Technology Centre, where it completed its environmental test campaign over the course of November 2025. There, the results obtained through the present analysis were utilized in the effort to select the appropriate temperatures of the Thermal Vacuum (TVAC) test of ERMIS-3, in a way which ensured that during the hot and cold extremes of the TVAC test, no component

of the satellite would violate its allowable temperature limits, while at the same time simulating the expected orbital thermal conditions in a manner that is as representative as possible.

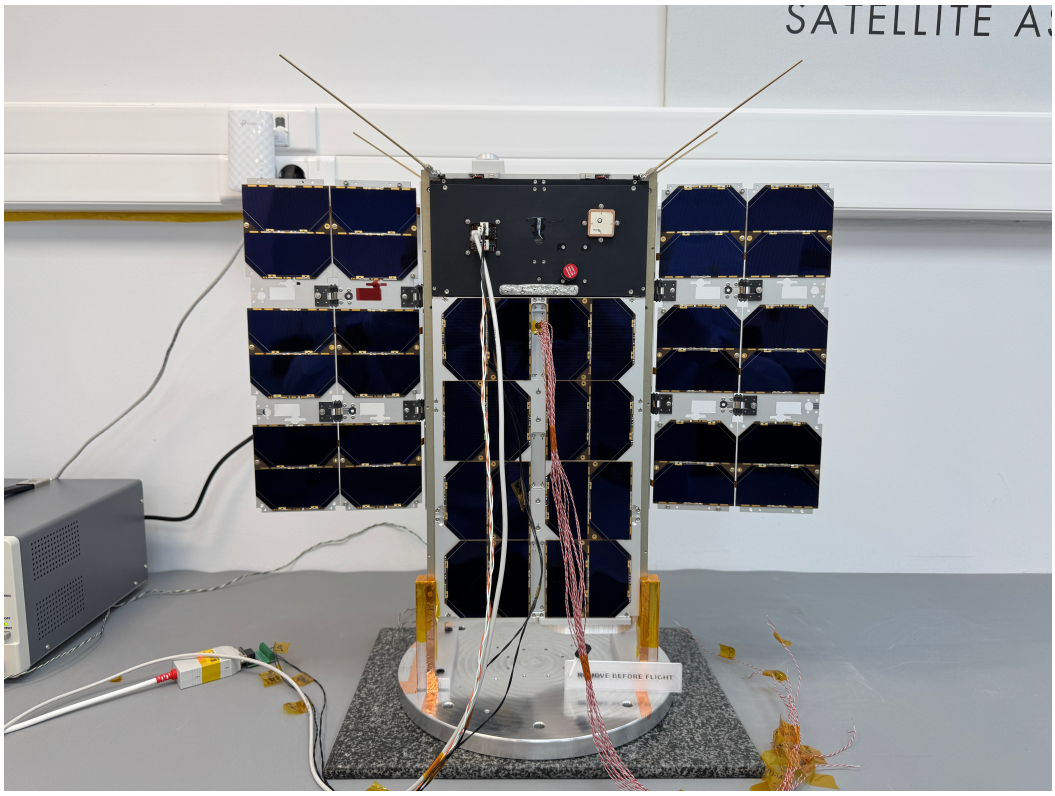

Figure 23. ERMIS-3 in its deployed configuration. Image credit: NKUA/Georgios Tzanoulinos.

In December 2025, ERMIS-3 was integrated into its EXOpod Nova CubeSat dispenser flight unit [69] at the facilities of Exolaunch GmbH (Berlin, Germany). ERMIS-3 was launched successfully on SpaceX's Transporter-16 dedicated smallsat rideshare mission on 30 March 2026 at 11:02:00 Coordinated Universal Time (UTC) [70]. Following the successful launch, ERMIS-3 was deployed from the second stage of the Falcon 9 rocket at the T+00:56:36 timepoint of the mission. The satellite's beacon signals were detected during the next orbit by the ground station operated by the NKUA in Psachna, Evia, Greece, confirming that it is operational, while stable communications with the satellite were established over its next passes. The ERMIS team then proceeded with the next objectives of the Launch and Early Orbit Phase of the mission and the commissioning of the satellite, before eventually transitioning to nominal operations.

Some COTS components present onboard ERMIS-3 are equipped with one or more integrated temperature sensors, which allow the ERMIS mission team to downlink component temperatures as part of the satellite's telemetry. Thus, the present section is dedicated to the presentation of a comparison between the results obtained during the FE thermal analysis of ERMIS-3 and the in-orbit measured temperatures of some vital components of the satellite. The components included in this comparison are the NanoMind A3200 OBC of ERMIS-3, the NanoCom AX100 half-duplex software configurable radio transceiver used for TT&C operations, as well as the two NanoPower BP8 Li-ion battery packs and the NanoPower P80 EPS of ERMIS-3.

The results of this temperature comparison are presented in Figure 24 and correspond to Sun-tracking and safe mode operations. More specifically, Figure 24a presents the temperature of the NanoMind A3200 OBC of ERMIS-3, Figure 24b presents the temperature of the NanoCom AX100 radio transceiver measured at two separate points by different

sensors, Figure 24c presents the temperatures of the two NanoPower BP8 Li-ion battery packs, while Figure 24d, Figure 24e, and Figure 24f are dedicated to the temperatures of the PMU, ACU (measured at different points by two separate sensors), and PDU of the NanoPower P80 EPS of ERMIS-3, respectively. The maximum and minimum allowable operational temperature limits of each component are also plotted in each subfigure using a red continuous line, and the data presented for all the examined components covers the first days after the deployment of ERMIS-3 on 30 March 2026, up until 30 May 2026. The predicted temperature limits presented in this comparison correspond to Sun-tracking and safe mode operations and were formed by synthesizing the maximum predicted temperature of each component extracted from the simulation that combines Sun-tracking or safe mode operations and "Hot" orbital thermal conditions regarding the upper end, and the minimum predicted temperature extracted from the simulation that combines Sun-tracking or safe mode operations and "Cold" orbital thermal conditions regarding the lower end. This way, a broader predicted temperature range that encompasses all possible scenarios of Sun-tracking and safe mode operations, respectively, is generated.

It should be noted that because component sensor accuracy specifications are not disclosed, and because precise internal placement and sensor/component interface details are unknown for most of the examined components, this comparison is confined to the evaluation of the measured temperatures against the maximum and minimum predicted temperatures and component operational limits, rather than also including a statistical analysis of the measurements and their error metrics.

Firstly, by observing the results that correspond to Sun-tracking, it is visible that the measured temperatures of the NanoMind A3200 OBC sit squarely within the predicted temperature range. Moreover, the same is largely true for the temperature measurements of the NanoCom AX100, where a notable spike in the measured temperature can be observed at the points where the component switches into transmission mode, a result that is expected and can be attributed to the increased electrical power consumption of this mode of operation. Despite the fact that the heat dissipation of the NanoCom AX100 was modeled in an orbit-averaged manner, it can be observed that on average, the in-orbit measured temperatures of the component are still clustered close to the center of the predicted temperature range, indicating that this simplified modeling approach along with the consideration of conservative 10 °C margins is an acceptable approximation of its thermal behavior.

Similarly, by reviewing the temperature measurements of the two NanoPower BP8 Li-ion battery packs, it can clearly be seen that when in Sun-tracking mode, there is still a considerable margin from the 2 °C limit where the electrical heating elements would be activated. This validates the previously presented results of the simulation according to which it was expected that no heater activation would be required during nominal Sun-tracking operations. It is also worth noting that the measured temperatures of the battery packs are noticeably shifted towards the minimum predicted temperature range for Sun-tracking operations. This is an expected result, as the presented maximum predicted temperature also accounts for increased heating effects due to Li-ion cell degradation, a phenomenon that is expected to occur progressively as the satellite's mission continues. Regarding the in-orbit temperatures of the three NanoPower P80 EPS sub-units during Sun-tracking operations, these are all at comparable levels and are again located close to the middle of the predicted temperature range.

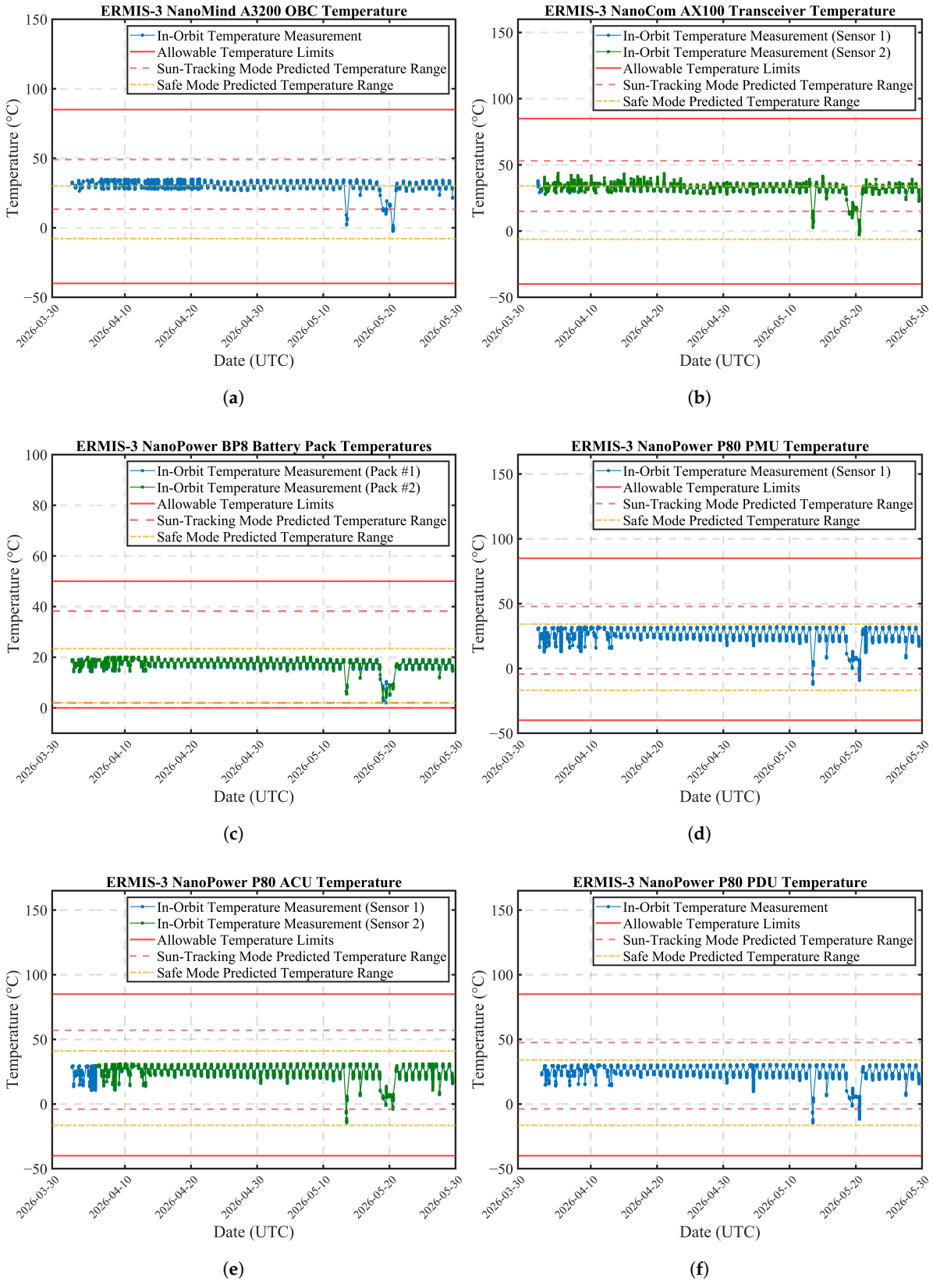

Figure 24. A comparison between the in-orbit temperatures of some critical subsystems of ERMIS-3, the corresponding temperature ranges predicted by the FE thermal model of the satellite and the allowable operational temperature limits of each component. (**a**) For the NanoMind A3200 OBC. (**b**) For the NanoCom AX100 radio transceiver. (**c**) For the two NanoPower BP8 Li-ion battery packs. (**d**) For the PMU of the NanoPower P80 EPS. (**e**) For the ACU of the NanoPower P80 EPS. (**f**) For the PDU of the NanoPower P80 EPS.

On two separate occasions, ERMIS-3 entered a safe mode of operation. More specifically, this happened on 13 May 2026 and in the period between 18 and 21 May 2026, with the satellite successfully recovering and, continuing its nominal operations henceforth. As a result, some data on its thermal behavior in this operating mode are also available. It should be noted, however, that these measurements cover only a small fraction of the satellite's operation, and coupled with the randomness of the satellite's attitude during safe mode, do not enable the extraction of confident conclusions. Nonetheless, by reviewing the safe mode's in-orbit temperature data, it is visible that, like in the Sun-tracking case, a good correlation between the thermal model predictions and the in-orbit temperature measurements can be observed, as all the recorded temperatures lay within the predicted temperature range for the safe mode cases. Furthermore, of significant interest in the safe mode case are the temperatures of the two NanoPower BP8 Li-ion battery packs, where it is seen that, as predicted by the satellite's FE thermal model, the activation of the heating elements at the threshold of 2 °C was indeed required in some of the orbits when the satellite operated in safe mode.

When observing the recorded in-orbit temperature measurements (especially the ones concerning the Sun-tracking mode), it is clear that they fall within a considerably narrower band compared to the worst-case envelope predicted by the FE model. There are two primary reasons for this result. Firstly, the actual sensors capture localized temperature measurements, while the FE simulation evaluates the temperature extremes in the entirety of the volume that represents the component. Secondly, in-orbit telemetry is sampled primarily during passes over the ground station, thereby capturing operational temperature snapshots rather than a full picture of the temperature evolution during the orbit. Nevertheless, the measured temperatures are well bounded within the upper and lower predicted temperature bounds, demonstrating a general consistency between the FE thermal model's predicted worst-case envelope and the in-orbit data. More crucially, the fact that the recorded in-orbit temperatures are located near the center of the predicted range and remain safely clear of the worst-case predicted temperature extremes highlights the intentionally conservative modeling and simulation approach that was followed, which included the bracketing of the problem using combinations of extreme possible orbital parameters (LTAN) and orbital thermal conditions, and also included the application of a 10 °C uncertainty margin over the calculated temperature extremes. This approach guarantees operational safety across all phases of the mission.

8. Discussion and Conclusions

To summarize the procedure followed for the thermal modeling and analysis of ERMIS-3, the overall methodology is structured herein as a step-by-step execution framework:

1. Data Collection & Material Definition: Based on information regarding the satellite's individual components, the physical, thermal, and optical properties of all appropriate materials and surfaces were collected through a review of relevant literature.
2. Geometric Modeling & Idealization: An idealized CAD model of the CubeSat was developed based on the detailed CAD model, ensuring it remained representative of the actual satellite in terms of component placement, primary geometric features, critical thermal interfaces, and mass.
3. Property Assignment & Interface Modeling: Appropriate thermal, physical, and optical properties were assigned to the model's constituents, followed by the assignment of contact joint heat-transfer coefficients.
4. Component Heat Dissipation & Dynamic Load Modeling: The heat dissipation of active components was modeled using specific electrical power consumption and efficiency data. Moreover, the heat dissipation of select EPS components was modeled

dynamically, using as a baseline the electrical power generated by the solar cells of the satellite. Finally, implicit events were set up to control the activation and deactivation of electrical heating elements based on set temperature thresholds.

5. Discretization & Model Verification: The idealized geometric model of ERMIS-3 was then discretized into finite elements and verified through rigorous convergence studies and energy balance checks.
6. Orbital Thermal Environment Definition: The orbital thermal environment and the satellite orbit were modeled using expected mission orbital elements and thermal conditions reported in published works of similar missions and handbooks. To cover any possible scenario, the problem was bracketed using the most extreme possible combinations of orbital parameters and thermal conditions, based on the expected orbit.
7. Result Extraction & Margin Philosophy: The maximum and minimum temperatures calculated for each component by the FE model for each simulated case were used in the evaluation of the satellite's thermal design. Moreover, based on standard industry practice, a margin was applied to the maximum and minimum calculated temperatures (leading to the predicted temperatures) in order to cover uncertainties that stem from aspects such as thermal/optical property uncertainty, thermal contact uncertainty, modeling errors, and the effect of the space environment on the materials of the satellite during the course of the mission. In general, the exact value of this margin is calculated based on applicable standards, the level of project maturity, possible qualification thresholds, and the availability of relevant test data. The predicted results of the analysis were then compared with the allowable temperature limits set by the component manufacturers.

From the results of the simulated thermal cases that are presented, it is obvious that no operational component of ERMIS-3 violates its allowable operational temperature limits, and no non-operational component surpasses its allowable non-operational temperature limits under any of the considered scenarios. The inclusion of a 10 °C uncertainty margin at both ends of the calculated temperature range also served as a conservative addition to the satellite's thermal design, which led to a high level of confidence regarding the satellite's ability to withstand and effectively operate in the thermal environment it is set to face in orbit. These results, along with the low duty cycle calculated for the battery pack electrical heating elements, also indicated that the satellite's passive thermal design is capable of maintaining the Li-ion battery cell temperatures within the allowable limits in the vast majority of situations, with only a small involvement of active elements in the coldest possible operational scenario. This result is indicative of a versatile thermal design that also facilitates electrical energy savings. Moreover, the use of the thermal analysis software to calculate the electrical power that is generated by the solar arrays of the satellite also serves as a computational-resource-efficient addition that enables modeling of the EPS heat dissipation in a realistic manner, under any possible satellite attitude scenario.

The aggressive timeline of the ERMIS Hellenic CubeSat Demonstration Mission precluded the detailed experimental validation of the thermal design and the thermal model of the CubeSat ERMIS-3 during the environmental test campaign of the mission. Consequently, the final FE thermal model of the satellite relied entirely on literature-sourced thermal, physical, optical, and thermal contact properties. Despite this setback, the in-orbit telemetry acquired after the launch of ERMIS-3 revealed a strong correlation between the predicted temperature ranges and the actual in-orbit temperatures, for several mission-critical platform subsystems. These results highlight the maturity of the currently available literature, as well as the robustness of standard industry practices and guidelines that have been set in the field of thermal design and analysis of satellites. As a result, for the development of typical CubeSat missions, an accurate thermal design derived solely from

computational engineering tools and literature-sourced property values appears to be increasingly viable. However, it should be acknowledged that limitations to the framework applied in this work also exist. For example, in cases of larger and more complex spacecraft, or in cases of small satellites and CubeSats where high-precision, temperature-sensitive components are present onboard, the application of conservative temperature margins may not be sufficient to accurately capture the spacecraft's thermal behavior, and the measurement of actual material thermal, physical, and optical properties, as well as the experimental correlation and calibration of the FE thermal model during the environmental test campaign, remain crucial.

Author Contributions: Conceptualization, K.-P.B.; methodology, K.-P.B.; software, K.-P.B.; validation, K.-P.B.; formal analysis, K.-P.B.; investigation, K.-P.B.; resources, V.L. and V.K.; data curation, K.-P.B.; writing—original draft preparation, K.-P.B.; writing—review and editing, V.L. and V.K.; visualization, K.-P.B.; supervision, V.L. and V.K.; project administration, V.L. and V.K.; funding acquisition, V.L. and V.K. All authors have read and agreed to the published version of the manuscript.

Funding: The work presented in this article has been carried out within the framework of the ERMIS Hellenic CubeSat Demonstration Mission, which has been funded by the European Space Agency (ESA) through the ESA Contract No. 4000140732/23/NL/ND.

Institutional Review Board Statement: Not applicable.

Data Availability Statement: The data presented in this study are available on request from the corresponding author due to research contract restrictions.

Acknowledgments: During the preparation of this work, the authors used Gemini 3 Flash Large Language Model (developed by Google), for language editing and typographical mistake detection, manuscript formatting in LaTeX (including bibliography styling according to the journal guidelines), and generating sections of MATLAB (version R2024a) code for data plotting and visualization. After using this tool, the authors reviewed and edited the content as needed and take full responsibility for the content of the publication.

Conflicts of Interest: The authors declare no conflicts of interest.

Abbreviations

The following abbreviations are used in this manuscript:

ACU	Array Conditioning Unit
ADCS	Attitude Determination and Control System
ASTM	American Society for Testing and Materials
BOL	Beginning-of-Life
CAD	Computer Aided Design
COMM	Communication System
COTS	Commercial Off-The-Shelf
DIN	Deutsches Institut für Normung (German Institute for Standardization)
DSP	Deployable Solar Panel
ECSS	European Cooperation for Space Standardization
EPS	Electrical Power System
ESA	European Space Agency
FE	Finite Element
FR4	Flame Retardant Type 4
FSO	Free-Space Optics
GNSS	Global Navigation Satellite System
IR	Infrared
LEO	Low Earth Orbit
Li-ion	Lithium-ion

LTAN	Local Time of Ascending Node
MPPT	Maximum Power Point Tracking
MSP	Modular Solar Panel
NASA	National Aeronautics and Space Administration
NKUA	National and Kapodistrian University of Athens
OBC	Onboard Computer
PCB	Printed Circuit Board
PDPU	Payload Data Processing Unit
PDU	Power Distribution Unit
PMU	Power Management Unit
SSO	Sun-Synchronous Orbit
TT&C	Telemetry, Tracking & Command
TVAC	Thermal Vacuum
UHF	Ultra-High Frequency
UTC	Coordinated Universal Time

Appendix A. Additional Modeling Details

Appendix A.1. Dynamic Heat Dissipation Profiles

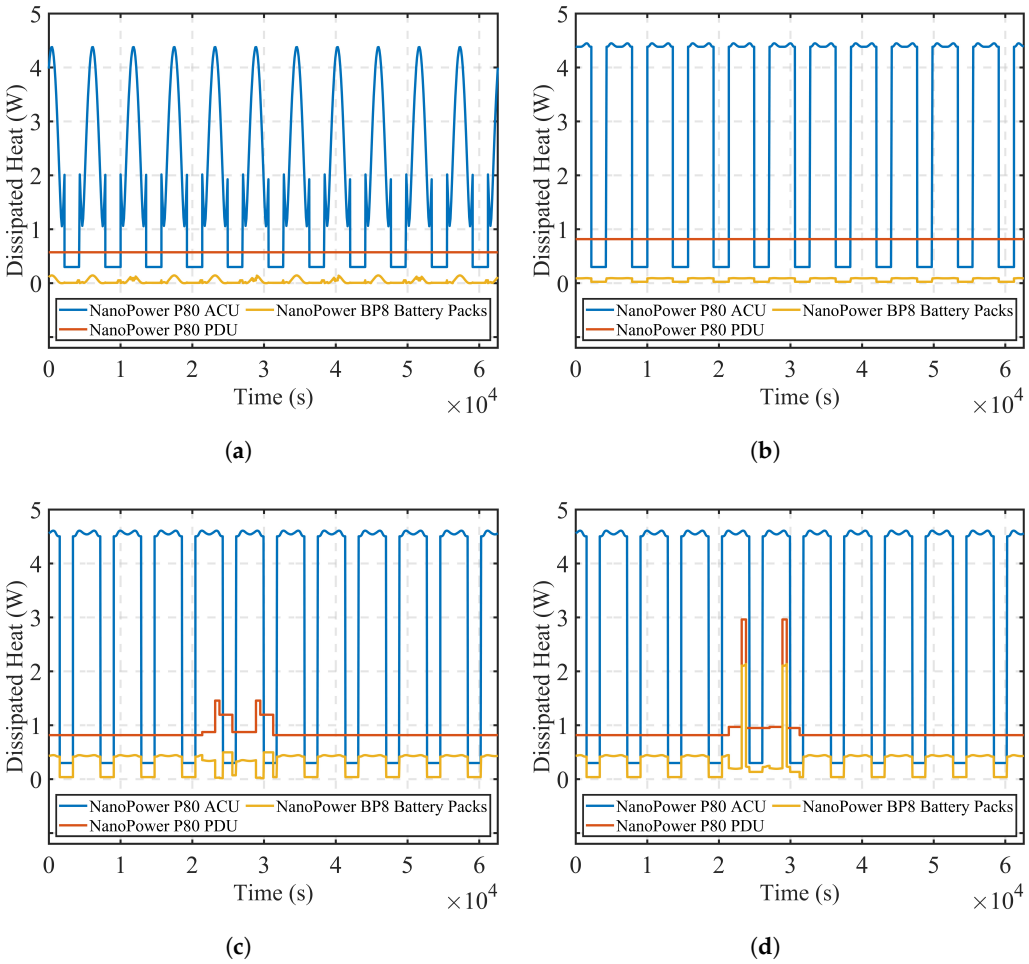

Figure A1. The dynamic heat dissipation profiles of the Li-ion battery, the ACU, and the PDU of ERMIS-3. (**a**) For the safe mode and "Cold" orbit scenario. (**b**) For the Sun-tracking mode and "Cold" orbit scenario. (**c**) For the hyperspectral imaging mode and "Hot" orbit scenario. (**d**) For the laser-optical communications link mode and "Hot" orbit scenario.

Figures A1 and A2 illustrate the dynamic heat dissipation profiles of the ERMIS-3 systems. Regarding the Li-ion battery packs, the total heat dissipation is assumed to be distributed evenly between the two units, which work in parallel.

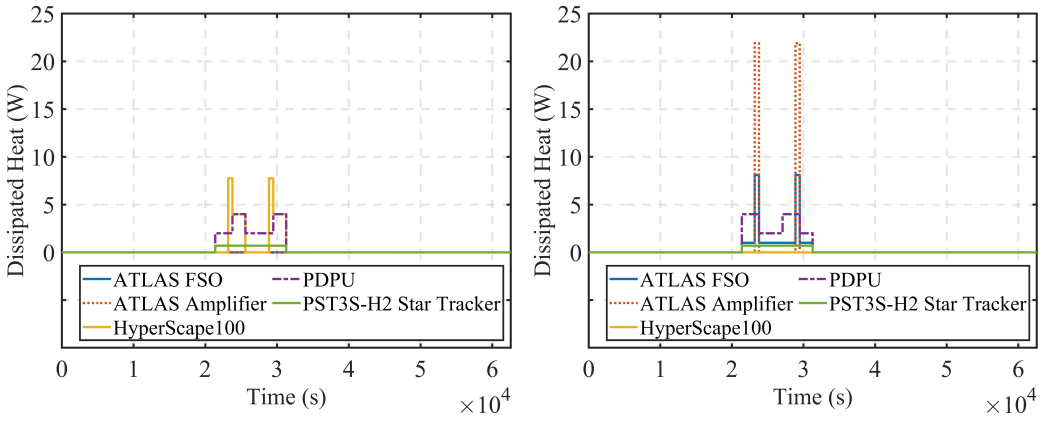

Figure A2. The heat dissipation profiles of the ATLAS FSO Assembly, ATLAS Amplifier Assembly, HyperScape100, PDPU, and PST3S-H2 Star Tracker of ERMIS-3. (**a**) During the hyperspectral imaging mode. (**b**) During the laser-optical link mode.

Appendix A.2. The Effect of Thermal Contact Uncertainty on Component Temperatures

To evaluate the effect of thermal contact uncertainty on the results provided by the FE thermal model, different thermal balance analyses of ERMIS-3 were set up. In these analyses it was assumed that the CubeSat orbits the Earth in a way that renders it permanently exposed to 1367 W/m^2 (equinox conditions) of solar radiation, while a 0.25 albedo factor and a 218 W/m^2 Earth IR radiation flux were also considered. The orientation and the internal heat dissipation (excluding that of the payloads) of the satellite in these simulations corresponded to Sun-tracking mode. To directly assess the effect of the contact joint heat-transfer coefficient values on the payloads of the satellite, the maximum and minimum temperatures of the four mission-enabling payloads of ERMIS-3 were evaluated at the end of a six-orbit period (total time of 34,136 s) for three different cases regarding each payload, namely the case that corresponds to the baseline contact joint heat-transfer coefficients between the payload and the satellite structure, as described in Table 3, a case where the contact joint heat-transfer coefficients of the payload in question are 50% higher than the baseline, and a case where the assumed contact joint heat-transfer coefficients of the payload are 50% lower than the baseline. In all simulated cases, each payload that is assumed to operate dissipates the maximum nominal heat reported in Table 6, while the other payloads remain deactivated and the heat of the EPS (battery and PDU) is not adjusted to match component operation, so as to not interfere with the obtained results. The results of these thermal balance analyses are summarized in Table A1.

Based on these results, it can be concluded that the calculated payload temperatures exhibit a modest sensitivity to the variations in contact joint heat-transfer coefficients (and by extension thermal contact conductance). As expected, in all simulated cases a lower contact joint heat-transfer coefficient yields higher component balance temperatures due to reduced thermal conduction toward the satellite's main structure, while a higher contact joint heat-transfer coefficient enhances conductive heat transfer from the component to the structure, leading to slightly lower balance temperatures. Quantitatively, the effect of a 50% variation in the baseline contact joint heat-transfer coefficient can be considered modest in this case, as the difference in calculated temperatures does not surpass 3.25 °C, relative to the baseline value. Furthermore, given the representative mounting and interface

characteristics of these payloads, these findings provide a reasonable basis to assume that other components across ERMIS-3 will exhibit a similarly modest sensitivity to variations in their contact joint heat-transfer coefficients. As a result, it was concluded that the 10 °C margin applied to all the calculated temperatures of the simulated operational cases of ERMIS-3 can cover this uncertainty in a reliable manner.

Table A1. Thermal sensitivity analysis results for ERMIS-3 payloads showing the minimum and maximum calculated temperatures under baseline, −50%, and +50% contact joint heat-transfer coefficient variations during thermal balance simulation.

Payload	50% Lower Contact Joint Heat-Transfer Coefficient		Baseline Contact Joint Heat-Transfer Coefficient		50% Higher Contact Joint Heat-Transfer Coefficient	
	Min. Temp. (°C)	Max. Temp. (°C)	Min. Temp. (°C)	Max. Temp. (°C)	Min. Temp. (°C)	Max. Temp. (°C)
ATLAS FSO Unit	47.55	49.60	46.53	48.70	46.14	48.39
ATLAS Amplifier Unit	61.80	63.06	58.82	60.17	57.71	59.12
PDPU	47.90	55.99	44.67	53.87	43.34	53.08
HyperScape100	15.76	62.02	15.32	60.76	15.20	60.27

Appendix B. Thermal FE Model Verification

To verify the numerical accuracy of the FE thermal model of ERMIS-3, mesh and radiation solver convergence studies were performed. Specifically, a thermal balance analysis of the satellite was set up, where it was assumed that the satellite orbits the Earth in such an orbit that it is permanently exposed to 1367 W/m^2 (equinox conditions) of solar radiation, while a 0.25 albedo factor and a 218 W/m^2 Earth IR radiation flux were also considered. The orientation and the internal heat dissipation of the satellite corresponded to Sun-tracking mode. To assess the convergence of the model, the average temperature of the entire CubeSat and the average temperatures of seven critical components were evaluated at the end of a six-orbit period (total time of 34,136 s).

To evaluate mesh independence, seven different mesh densities (ranging from 99,800 to 393,678 domain elements) were examined. Table A2 presents the results of this study, where an increase in mesh density from 169,653 to 262,657 elements (an increase of more than 50%) yields minor temperature changes of 0.21 °C or less across all examined components (a relative change that is less than 0.07% in terms of absolute temperature), while further mesh refinement up to 393,678 elements (approximately 50% increase) produces negligible temperature changes of less than 0.07 °C across all examined components. As a result, the mesh comprised of 262,657 elements was selected for all subsequent analyses, in order to achieve a balance between accuracy and computational efficiency. The detailed breakdown of these domain elements is presented in Table A3.

Table A2. The results of the mesh convergence study of ERMIS-3.

Domain Elements	Component Average Thermal Balance Temperature (°C)							
	Satellite Average	NanoMind A3200	Li-Ion Cells	NanoPower P80 EPS	HyperScape 100	ATLAS FSO Unit	ATLAS Amplifier Unit	PDPU
99,800	36.83	48.46	37.16	43.75	27.04	37.20	29.48	39.60
123,133	36.80	48.46	37.19	43.79	26.78	37.14	29.44	39.51
169,653	36.99	48.64	37.50	44.07	27.11	37.35	29.54	39.77
216,915	37.02	48.71	37.56	44.24	27.03	37.38	29.51	39.84
262,657 *	37.02	48.72	37.60	44.28	26.98	37.39	29.50	39.86
320,840	37.05	48.74	37.62	44.33	27.01	37.43	29.51	39.88
393,678	37.06	48.78	37.63	44.35	27.01	37.43	29.52	39.89

* Element number eventually used for the FE thermal analyses of ERMIS-3.

Table A3. The types and total number of domain elements used for the thermal simulations of ERMIS-3.

Element Type	Element Number
Tetrahedra	209,782
Pyramids	5404
Prisms	34,007
Hexahedra	13,464
Total	262,657

To examine the convergence of the Ray-Shooting radiation simulation method, four different radiation resolution settings (4, 8, 16, and 32) were examined using the selected mesh of 262,657 domain elements. In that regard, Table A4 presents the resulting satellite and component average thermal balance temperatures, where it is visible that doubling the radiation resolution from 4 to 8 leads to minor temperature variations of 0.34 °C or less across all the examined components (a relative change that is 0.11% or less in terms of absolute temperature). Further doubling of the resolution to 16 yielded negligible shifts in the average temperatures, equal to or less than 0.04 °C (less than 0.015% in terms of absolute temperature), while quadrupling the resolution from 8 to 32 yielded a maximum temperature difference of 0.13 °C (less than 0.05% in terms of absolute temperature). These results demonstrate that the default radiation resolution configuration of 8 provides sufficient numerical accuracy for this application and was therefore maintained for all the thermal simulations of ERMIS-3.

Table A4. The results of the radiation resolution convergence study.

Radiation Resolution	Component Average Thermal Balance Temperature (°C)							
	Satellite Average	NanoMind A3200	Li-Ion Cells	NanoPower P80 EPS	HyperScape 100	ATLAS FSO Unit	ATLAS Amplifier Unit	PDPU
4	36.81	48.49	37.38	44.06	26.64	37.19	29.30	39.64
8 *	37.02	48.72	37.60	44.28	26.98	37.39	29.50	39.86
16	37.04	48.75	37.60	44.30	27.02	37.41	29.52	39.88
32	37.05	48.85	37.60	44.32	27.03	37.42	29.52	39.89

* The default configuration and the one eventually used in the FE thermal analyses of ERMIS-3.

To evaluate the temporal discretization and stability of the transient simulations, cases with different time point densities per orbit were simulated. In that regard, Figure A3 illustrates the average temperature of ERMIS-3 while in Sun-tracking mode during "Cold"

orbital thermal conditions for a period of three orbits, for cases utilizing 25, 50, and 100 time points per orbit, respectively. As demonstrated by the nearly overlapping temperature plots, the transient solution exhibits good stability and, in practical terms, independence from the chosen temporal resolution, with the maximum temperature difference observed between the 50 and 100 time point cases never exceeding 0.2 °C, a difference that is less than 0.075% in terms of absolute temperature. As a result, a temporal discretization of 50 time points per orbit was chosen in the thermal analysis of ERMIS-3 to maintain a balance between computational overhead and accuracy.

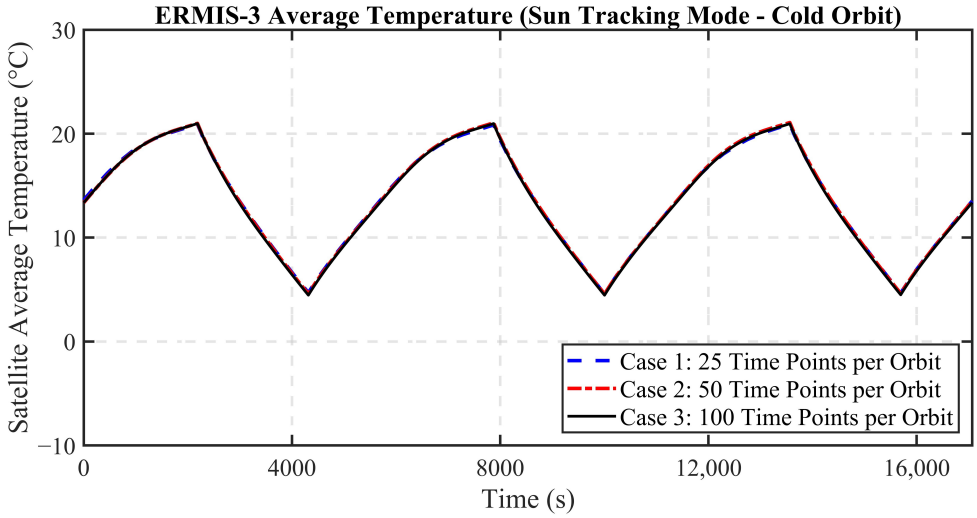

Figure A3. The evolution of the average temperature of ERMIS-3 under Sun-tracking mode, as calculated by its thermal FE model using different temporal resolutions in a transient analysis.

Finally, to verify that the FE model's energy balance (absorbed and generated thermal energy compared to rejected and stored thermal energy) is correct, an energy balance study was performed on the results of the scenario that combines "Hot" orbital thermal conditions with the laser optical communications mode. The primary reason for this choice was the fact that this mode also includes high heat dissipation by internal components (ATLAS and PDPU) that are activated and deactivated dynamically. This energy balance simulation covers a period of 13 complete orbits, and its results are presented in Figure A4. As shown in the figure, the energy balance curve remains tightly bounded around zero for most of the simulation. The notable positive and negative spikes seen at certain points correspond to orbital eclipse transitions (eclipse in and out), where there is an abrupt change in the solar band radiation that is incident to the model. These spikes reach values of up to 3.96 W, which is approximately 1.39% of the solar band radiative power that is incident to the satellite's surfaces at the start or end of an eclipse, which stands at 285.59 W. Moreover, some distinct localized transients of small magnitude occur during the activation of the laser-optical communication payloads (approximately after the 32,000 s time point). These transient deviations progressively drop and eventually settle at values that are nearly equal to zero. Furthermore, by calculating the trapezoidal time-weighted average of the thermal energy balance curve, it was found that the deviation from zero is on average 0.0002 W throughout the entire 13-orbit period. These results confirm that the FE thermal model of ERMIS-3 conserves thermal energy and that the boundary conditions, internal heat dissipation and the numerical solver loads have been correctly coupled and are numerically stable.

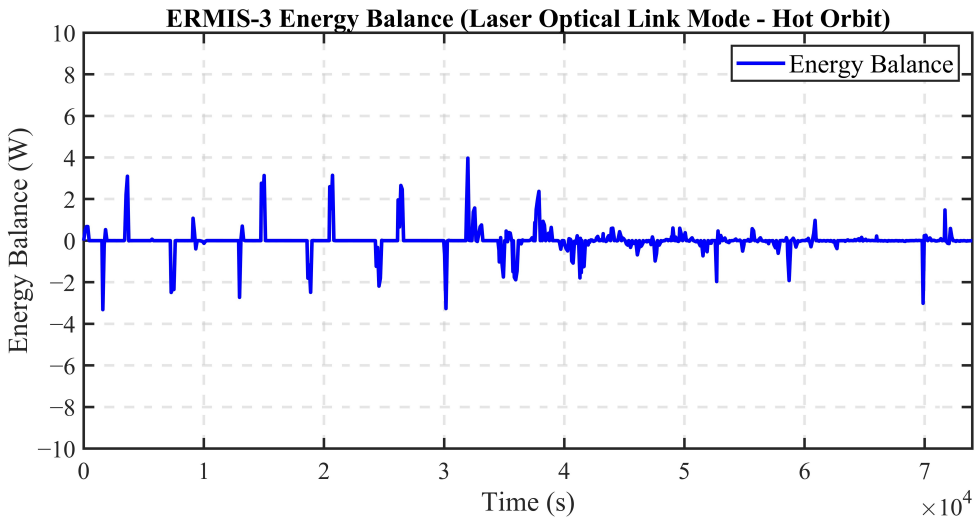

Figure A4. The results of the thermal energy balance verification study performed for the FE model of ERMIS-3.

Appendix C. Supplementary Thermal Analysis Result Tables

Table A5 presents a summary of all the temperatures of the components of ERMIS-3 when operational, for all four simulated combinations of operating modes and orbital thermal conditions, compared to the allowable operational temperature limits of each component. In a similar manner, Table A6 summarizes the temperatures of the components of ERMIS-3 when non-operational, for all four simulated combinations of operating modes and orbital thermal conditions, compared to the allowable non-operational temperature limits of each component.

Table A5. The minimum and maximum predicted temperatures for each operating component of ERMIS-3 across all four simulated cases, compared to its maximum and minimum allowable operational temperature limits.

Component	Min. Allowable Operational Temperature (°C)	Margin Remaining to Cold Limit (°C)	Component Predicted Operational Temperature (°C)		Margin Remaining to Hot Limit (°C)	Max. Allowable Operational Temperature (°C)
			Min.	Max.		
OBC and TT&C						
NanoMind A3200	−30	22.22	−7.78	52.29	32.71	85
NanoDock DMC−3	−40	29.65	−10.35	55.20	29.80	85
NanoCom AX100	−30	23.80	−6.20	56.01	28.99	85
NanoCom ANT−6F	−40	5.70	−34.30	68.11	16.89	85
GNSS						
Calian TW1322	−40	30.70	−9.30	56.11	28.89	85
NovAtel OEM719	−40	60.70	20.70	65.76	19.24	85
COMM						
NanoCom ANT8250	−35	-	-	-	-	75
NanoCom ANT2150	−40	-	-	-	-	85
NanoCom Link SX	−40	-	-	-	-	85

Table A5. *Cont.*

Component	Min. Allowable Operational Temperature (°C)	Margin Remaining to Cold Limit (°C)	Component Predicted Operational Temperature (°C)		Margin Remaining to Hot Limit (°C)	Max. Allowable Operational Temperature (°C)
			Min.	Max.		
ADCS						
Depl. Magnetometer	−20	0.52	−19.48	38.79	41.21	80
Cmpct. Magnetometer	−20	1.30	−18.70	44.72	35.28	80
CubeNode	−20	26.19	6.19	44.92	35.08	80
Star Tracker	−40	44.85	4.85	44.62	0.38	45
Earth Horizon Sensor	−20	1.05	−18.95	42.31	37.69	80
Fine Sun Sensor	−20	1.85	−18.15	56.68	23.32	80
CubeComputer	−20	8.35	−11.65	50.12	29.88	80
Magnetorquers	−20	0.75	−19.25	52.66	27.34	80
Reaction Wheels	−20	26.19	6.19	43.74	36.26	80
EPS						
Stack Breakout PCB	−30	18.95	−11.05	47.83	32.17	80
Solar Cells	−150	88.25	−61.75	81.24	68.76	150
NanoPower P80 EPS	−40	22.73	−17.27	61.53	23.47	85
NanoPower BP8 (Li-ion cells)	0	2.00	2.00	41.67	8.33	50
Payload						
ATLAS FSO Assembly	−25	32.55	7.55	44.63	15.37	60
ATLAS Amplifier Assembly	−25	37.62	12.62	45.28	14.72	60
HyperScape100	−10	2.40	−7.60	49.51	0.49	50
PDPU	−40	47.30	7.30	55.59	29.41	85

Table A6. The minimum and maximum predicted temperatures for each non-operating component of ERMIS-3 across all four simulated cases, compared to its maximum and minimum allowable non-operational temperature limits.

Component	Min. Allowable Non-Operational Temperature (°C)	Margin Remaining to Cold Limit (°C)	Component Predicted Non-Operational Temperature (°C)		Margin Remaining to Hot Limit (°C)	Max. Allowable Non-Operational Temperature (°C)
			Min.	Max.		
OBC and TT&C						
NanoMind A3200	−30	-	-	-	-	85
NanoDock DMC-3	−40	-	-	-	-	85
NanoCom AX100	−30	-	-	-	-	85
NanoCom ANT-6F	−40	-	-	-	-	90
GNSS						
Calian TW1322	−55	35.70	−19.30	27.38	67.62	95
NovAtel OEM719	−55	46.15	−8.85	17.27	77.73	95
COMM						
NanoCom ANT8250	−35	11.84	−23.16	37.03	42.97	80
NanoCom ANT2150	−40	14.87	−25.13	36.41	48.59	85
NanoCom Link SX	−40	23.10	−16.90	47.58	37.42	85

Table A6. *Cont.*

Component	Min. Allowable Non-Operational Temperature (°C)	Margin Remaining to Cold Limit (°C)	Component Predicted Non-Operational Temperature (°C)		Margin Remaining to Hot Limit (°C)	Max. Allowable Non-Operational Temperature (°C)
			Min.	Max.		
ADCS						
Depl. Magnetometer	−20	-	-	-	-	80
Cmpct. Magnetometer	−20	-	-	-	-	80
CubeNode	−20	2.10	−17.90	39.96	40.04	80
Star Tracker	−40	21.30	−18.70	39.05	5.95	45
Earth Horizon Sensor	−20	-	-	-	-	80
Fine Sun Sensor	−20	-	-	-	-	80
CubeComputer	−20	-	-	-	-	80
Magnetorquers	−20	-	-	-	-	80
Reaction Wheels	−20	8.73	−11.27	13.51	66.49	80
EPS						
Stack Breakout PCB	−30	-	-	-	-	80
Solar Cells	−150	-	-	-	-	150
NanoPower P80 EPS	−40	-	-	-	-	85
NanoPower BP8 (Li-ion cells)	−20	-	-	-	-	45
Payload						
ATLAS FSO Assembly	−40	23.86	−16.14	41.68	28.32	70
ATLAS Amplifier Assembly	−40	20.85	−19.15	35.06	34.94	70
HyperScape100	−25	5.50	−19.50	44.46	20.54	65
PDPU	−40	22.40	−17.60	45.40	39.60	85

References

1. Cappelletti, C.; Robson, D. CubeSat Missions and Applications. In *CubeSat Handbook*; Cappelletti, C., Battistini, S., Malphrus, B.K., Eds.; Academic Press: Cambridge, MA, USA, 2021; pp. 53–65. https://doi.org/10.1016/B978-0-12-817884-3.00002-3.
2. Bouzoukis, K.-P.; Moraitis, G.; Kostopoulos, V.; Lappas, V. An Overview of CubeSat Missions and Applications. *Aerospace* **2025**, *12*, 550. https://doi.org/10.3390/aerospace12060550.
3. ITP Engines UK Ltd. ESATAN-TMS Thermal Modeling Suite. Available online: https://www.esatan-tms.com/ (accessed on 23 August 2026).
4. Synopsys, Inc.; ANSYS, Inc. Ansys Thermal Desktop: Heat Transfer & Fluid Flow Modeling Software. Available online: https://www.ansys.com/products/fluids/ansys-thermal-desktop (accessed on 23 August 2026).
5. COMSOL Multiphysics®. Heat Transfer Module. Available online: https://www.comsol.com/heat-transfer-module (accessed on 23 August 2026).
6. Radian Space, S.L. Thermal Analysis in the Cloud. Available online: https://radian.systems/ (accessed on 23 August 2026).
7. NASA. State-of-the-Art of Small Spacecraft Technology, Chapter 7.0: Thermal Control. 2026. Available online: https://www.nasa.gov/smallsat-institute/sst-soa/thermal-control/ (accessed on 23 August 2026).
8. Garzón, A.; Tami, J.A.; Campos-Julca, C.D.; Acero-Niño, I.F. Effect of Beta Angle and Contact Conductances on the Temperature Distribution of a 3U CubeSat. *Therm. Sci. Eng. Prog.* **2022**, *29*, 101183. https://doi.org/10.1016/j.tsep.2021.101183.
9. Chandrashekar, S. Thermal Analysis and Control of MIST CubeSat. Master's Thesis, KTH Royal Institute of Technology, Stockholm, Sweden, 2017. Available online: https://kth.diva-portal.org/smash/record.jsf?pid=diva2%3A1071655&dswid=-1864 (accessed on 18 November 2026).
10. Blanchete, N.; Bah, A. CubeSat thermal analysis: Evaluating models for thermal contact conductance. *Heat Mass Transf.* **2024**, *60*, 1221–1233. https://doi.org/10.1007/s00231-024-03482-z.

11. Cisneros Ortega, J.C.; Martínez Sisniega, N.S.; Mendoza, U.A.; Rivas, R.O. Analysis of the temperature of a 1U CubeSat due to radiation in space. In Proceedings of the 2017 World Congress on Advances in Structural Engineering and Mechanics (ASEM17), Ilsan (Seoul), Republic of Korea, 28 August–1 September 2017. Available online: https://cdn.techno-press.org/i-asem/publication_conf/asem17/1.SM/W3A.4.SM2145_4343F1.pdf(accessed on 18 November 2026).
12. Foster, I. *Small Satellite Thermal Modeling Guide, AFRL20222564*; Air Force Research Laboratory, Space Vehicles Directorate: Kirtland Air Force Base, Albuquerque, NM, USA, 2022. https://doi.org/10.13140/RG.2.2.35225.29288.
13. Astrolight. ATLAS Laser Communication Terminal. Available online: https://astrolightspace.com/atlas/ (accessed on 23 August 2026).
14. Simera Sense. Earth Observation/xScape100/HyperScape100. Available online: https://simera-sense.com/products/hyperscape100/ (accessed on 23 August 2026).
15. GomSpace. Products. Available online: https://gomspace.com/products/ (accessed on 23 August 2026).
16. CubeSpace Satellite Systems. Integrated Turn-Key ADCS. Available online: https://www.cubespace.co.za/products/turnkey-adcs/ (accessed on 23 August 2026).
17. TY-Space Technology (Beijing) Ltd. Products/Star Trackers. Available online: https://www.ty-space.net/products/star-trackers/ (accessed on 23 August 2026).
18. Autodesk Inc. Products/Autodesk Inventor: Powerful 3D Mechanical Design Software. Available online: https://www.autodesk.com/products/inventor/overview (accessed on 23 August 2026).
19. *MIL-PRF-8625 Revision F Amendment 2*; Anodic Coatings for Aluminum and Aluminum Alloy. United States Department of Defense: The Pentagon, Arlington County, VA, USA, 2020. Available online: https://quicksearch.dla.mil/qsDocDetails.aspx?ident_number=7074 (accessed on 23 August 2026).
20. *MIL-DTL-5541 Revision F Notice 2*; Chemical Conversion Coatings on Aluminum and Aluminum Alloys. United States Department of Defense: The Pentagon, Arlington County, VA, USA, 2024. Available online: https://quicksearch.dla.mil/qsDocDetails.aspx?ident_number=5499 (accessed on 23 August 2026).
21. Miller, S.K.R. Tutorial on Atomic Oxygen Effects and Contamination (Document ID: 20170006623). In Proceedings of the Applied Space Environment Conference, Huntsville, AL, USA, 15–19 May 2017. Available online: https://ntrs.nasa.gov/citations/20170006623 (accessed on 23 August 2026).
22. *PC/104 Specification Version 2.6*; PC/104 Embedded Consortium: Sacramento, CA, USA, 2008. Available online: https://pc104.org/hardware-specifications/pc104/ (accessed on 23 August 2026).
23. *DIN 976-1:2016-09*; Fasteners—Stud Bolts-Part 1: Metric Thread. DIN Media GmbH: Berlin, Germany, 2016. Available online: https://www.dinmedia.de/de/norm/din-976-1/257277286 (accessed on 23 August 2026).
24. Clawson, J.F.; Tsuyuki, G.T.; Anderson, B.J.; Justus, C.G.; Batts, W.; Ferguson, D.; Gilmore, D.G. Chapter 2: Spacecraft Thermal Environments. In *Spacecraft Thermal Control Handbook. Volume 1, Fundamental Technologies*, 2nd ed.; Gilmore, D.G., Ed.; The Aerospace Press: El Segundo, CA, USA, 2002; pp. 21–69.
25. Peyrou-Lauga, R. Using Real Earth Albedo and Earth IR Flux for Spacecraft Thermal Analysis. In Proceedings of the 47th International Conference on Environmental Systems, Charleston, SC, USA, 16–20 July 2017. Available online: http://hdl.handle.net/2346/72957 (accessed on 18 November 2026).
26. Peyrou-Lauga, R. An enhanced Earth InfraRed flux and Albedo model based on real data. In Proceedings of the 51st International Conference on Environmental Systems, Saint Paul, MN, USA, 10–14 July 2022. Available online: https://hdl.handle.net/2346/89606 (accessed on 18 November 2026).
27. Appendix B: Material Thermal Properties. In *Spacecraft Thermal Control Handbook. Volume 1, Fundamental Technologies*, 2nd ed.; Gilmore, D.G., Ed.; The Aerospace Press: El Segundo, CA, USA, 2002; pp. 803–818.
28. MakeItFrom.com Material Properties Database. 6082 (AlSi1MgMn, 3.2315, H30, A96082) Aluminum. Available online: https://www.makeitfrom.com/material-properties/6082-AlSi1MgMn-3.2315-H30-A96082-Aluminum (accessed on 23 August 2026).
29. MakeItFrom.com Material Properties Database. 93–95% Purity Alumina (ASTM D2442 Type II, IEC 60672 Type C-786). Available online: https://www.makeitfrom.com/material-properties/93-95-Percent-Purity-Alumina-ASTM-D2442-Type-II-IEC-60672-Type-C-786 (accessed on 23 August 2026).
30. TPSX Materials Properties Database—NASA. Polyimide H-Film Kapton. Available online: https://tpsx.arc.nasa.gov/Material?id=965 (accessed on 23 August 2026).
31. Dou, Y.; Luo, J.; Qi, L.; Lian, H.; Huang, J. Drop-on-demand printing of recyclable circuits by partially embedding molten metal droplets in plastic substrates. *J. Mater. Process. Technol.* **2021**, *297*, 117268. https://doi.org/10.1016/j.jmatprotec.2021.117268
32. TPSX Materials Properties Database—NASA. Polycarbonate Various Fillers. Available online: https://tpsx.arc.nasa.gov/Material?id=960 (accessed on 23 August 2026).
33. MakeItFrom.com Material Properties Database. Unfilled PPS. Available online: https://www.makeitfrom.com/material-properties/Unfilled-PPS (accessed on 23 August 2026).

34. Ioffe Physical-Technical Institute of the Russian Academy of Sciences. $Ga_xIn_{1-x}P$ Thermal Properties. Available online: https://www.ioffe.ru/SVA/NSM/Semicond/GaInP/thermal.html (accessed on 23 August 2026).
35. Ioffe Physical-Technical Institute of the Russian Academy of Sciences. $Ga_xIn_{1-x}P$ Basic Parameters at 300 K. Available online: https://www.ioffe.ru/SVA/NSM/Semicond/GaInP/basic.html (accessed on 23 August 2026).
36. Drake, S.J.; Wetz, D.A.; Ostanek, J.K.; Miller, S.P.; Heinzel, J.M.; Jain, A. Measurement of anisotropic thermophysical properties of cylindrical Li-ion cells. *J. Power Sources* **2014**, *252*, 298–304. https://doi.org/10.1016/j.jpowsour.2013.11.107.
37. Kauder, L. *Spacecraft Thermal Control Coatings References*; NASA/TP-2005-212792; NASA Goddard Space Flight Center: Greenbelt, MD, USA, 2005. Available online: https://ntrs.nasa.gov/citations/20070014757 (accessed on 23 August 2026).
38. Narimane, B.; Bah, A. Thermal control: Case study of 3U CubeSat. In Proceedings of the 2023 Advances in Science and Engineering Technology International Conferences (ASET), Dubai, United Arab Emirates, 20–23 February 2023; pp. 1–5. https://doi.org/10.1109/ASET56582.2023.10180811.
39. Lucia, F. Development of a Tool for Thermal Analysis of Small Spacecrafts. Master's Thesis, Politecnico di Torino, Turin, Italy, 2023. Available online: https://webthesis.biblio.polito.it/27931/ (accessed on 18 November 2026).
40. Appendix A: Surface Optical Property Data. In *Spacecraft Thermal Control Handbook. Volume 1, Fundamental Technologies*, 2nd ed.; Gilmore, D.G., Ed.; The Aerospace Press: El Segundo, CA, USA, 2002; pp. 791–801.
41. Finckenor, M.M.; Coker, R.F. *Optical Properties of Nanosatellite Hardware*; NASA/TM—2014–218195; NASA Marshall Space Flight Center: Redstone Arsenal, Huntsville, AL, USA, 2014. Available online: https://ntrs.nasa.gov/citations/20140010335 (accessed on 23 August 2026).
42. The Engineering ToolBox. Emissivity Coefficients of Common Materials: Data & Reference Guide. Available online: https://www.engineeringtoolbox.com/emissivity-coefficients-d_447.html (accessed on 23 August 2026).
43. Seyedzadeh, A.; Okasha, M.; Alblooshi, A.; Aizat, W.F.; Jallad, A.H.; Sulaeman, E. Thermal analysis and experimental validation of the thermal subsystem of AlAinSat-1. *Egypt. J. Remote Sens. Space Sci.* **2025**, *28*, 185–204. https://doi.org/10.1016/j.ejrs.2025.03.002.
44. Gluck, D.F.; Baturkin, V. Chapter 8: Mountings and Interfaces. In *Spacecraft Thermal Control Handbook. Volume 1, Fundamental Technologies*, 2nd ed.; Gilmore, D.G., Ed.; The Aerospace Press: El Segundo, CA, USA, 2002; pp. 247–329.
45. Cooper, M.G.; Mikić, B.B.; Yovanovich, M.M. Thermal contact conductance. *Int. J. Heat Mass Transf.* **1969**, *12*, 279–300. https://doi.org/10.1016/0017-9310(69)90011-8.
46. Mikić, B.B. Thermal contact conductance; theoretical considerations. *Int. J. Heat Mass Transf.* **1974**, *17*, 205–214. https://doi.org/10.1016/0017-9310(74)90082-9.
47. Sridhar, M.R.; Yovanovich, M.M. Elastoplastic Contact Conductance Model for Isotropic Conforming Rough Surfaces and Comparison With Experiments. *ASME. J. Heat Transf.* **1996**, *118*, 3–9. https://doi.org/10.1115/1.2824065.
48. Boushon, K.E. Thermal Analysis and Control of Small Satellites in Low Earth Orbit. Master's Thesis, Missouri University of Science and Technology, Rolla, MO, USA, 2018. Available online: https://scholarsmine.mst.edu/masters_theses/7755 (accessed on 18 November 2026).
49. GomSpace. NanoPower MSP Datasheet: Modular Solar Panel with Integrated Sun Sensor and Temperature Sensor. Available online: https://gomspace.com/product/nanopower-msp/ (accessed on 24 August 2026).
50. GomSpace. NanoPower Deployable Solar Panel Datasheet: Deployable Solar Panel for 3U or 6U Satellite. Available online: https://gomspace.com/product/nanopower-dsp/ (accessed on 24 August 2026).
51. CESI S.p.A. Space Solar Cells/Low Cost Triple-Junction Solar Cell for Space Applications (CTJLC) Datasheet. Available online: https://www.cesi.it/space-solar-cells/ (accessed on 24 August 2026).
52. Koval, N.E.; Da Pieve, F.; Artacho, E. Ab *Initio* Electron. Stopping Power Protons $Ga_{0.5}In_{0.5}P$/GaAs/Ge Triple-Junction Sol. Cells Space Applications. *R. Soc. Open Sci.* **2020**, *7*, 200925. https://doi.org/10.1098/rsos.200925.
53. Cui, M.; Chen, N.; Yang, X.; Zhang, H. Fabrication and temperature dependence of a GaInP/GaAs/Ge tandem solar cell. *J. Semicond.* **2012**, *33*, 024006. https://doi.org/10.1088/1674-4926/33/2/024006.
54. Landis, G.A. Review of solar cell temperature coefficients for space. In Proceedings of the 13th Space Photovoltaic Research and Technology Conference (SPRAT 13), Cleveland, OH, USA, 1 September 1994. Available online: https://ntrs.nasa.gov/citations/19950014125 (accessed on 24 August 2026).
55. Cao, M.; Zhang, T.; Liu, Y.; Yu, W.; Ming, M. A performance degradation model of solar cells in an on-orbit resource satellite based on peak currents. *Sol. Energy* **2019**, *189*, 26–34. https://doi.org/10.1016/j.solener.2019.07.030.
56. Abagero, A.; Abebe, Y.; Tullu, A.; Jung, Y.S.; Jung, S. Deep Learning-Based MPPT Approach to Enhance CubeSat Power Generation. *IEEE Access* **2025**, *13*, 40076–40089. https://doi.org/10.1109/ACCESS.2025.3546066.
57. GomSpace. NanoPower P80 Datasheet. Available online: https://gomspace.com/product/nanopower-p80/ (accessed on 25 August 2026).
58. GomSpace. NanoPower BP8 Datasheet. Available online: https://gomspace.com/product/nanopower-bp8/ (accessed on 25 August 2026).

59. Fischer, M.; Brand, M.J.; Karger, A.; Gomez, M.R.; Rehm, M.; Natterer, J.; Jossen, A. How degradation of lithium-ion batteries impacts capacity fade and resistance increase: A systematic, correlative analysis. *J. Power Sources* **2025**, *656*, 237921. https://doi.org/10.1016/j.jpowsour.2025.237921.
60. Steiner, T.R. High temperature steady-state experiment for computational radiative heat transfer validation using COMSOL and ANSYS. *Results Eng.* **2022**, *13*, 100354. https://doi.org/10.1016/j.rineng.2022.100354.
61. NASA Goddard Space Flight Center. Cosmic Background Explorer (COBE). Available online: https://lambda.gsfc.nasa.gov/product/cobe/ (accessed on 25 August 2026).
62. Jaworske, D.A. Changes in the Optical Properties of Materials Are Observed After 18 Months in Low Earth Orbit. In *Research and Technology 1998*; NASA Lewis Research Center: Cleveland, OH, USA, 1999. Available online: https://ntrs.nasa.gov/citations/20050188450 (accessed on 1 November 2026).
63. Teichman, L.A.; Stein, B.A. *NASA/SDIO Space Environmental Effects on Materials Workshop, Part 1*; NASA Langley Research Center: Hampton, VA, USA, 1989. Available online: https://ntrs.nasa.gov/citations/19890014157 (accessed on 1 November 2026).
64. Scialdone, J.J.; Clatterbuck, C.H.; Ayres-Treusdell, M.; Park, G.; Kolos, D. *Atomic Oxygen and Space Environment Effects on Aerospace Materials Flown with EOIM-III Experiment (NASA Technical Memorandum NASA-TM-104636)*; NASA Goddard Space Flight Center: Greenbelt, MD, USA, 1996. Available online: https://ntrs.nasa.gov/citations/19970010450 (accessed on 1 November 2026).
65. European Cooperation for Space Standardization (ECSS). *ECSS-E-ST-31C–Thermal Control*; European Space Research and Technology Centre (ESTEC): Noordwijk, The Netherlands, November 2008. Available online: https://ecss.nl/standard/ecss-e-st-31c-thermal-control/ (accessed on 26 August 2026).
66. CubeSat Resources: Thermal Management. Available online: https://cubesat-resources.space/development/thermal/ (accessed on 31 October 2026).
67. Blanchete, N.; Bah, A. Thermal design, analysis and test: Framework for CubeSat in low Earth orbit. *Results Eng.* **2024**, *24*, 103401. https://doi.org/10.1016/j.rineng.2024.103401.
68. Wallace, P.; Kalapura, A.; Kim, S.I. Thermal Modelling and Analysis of a Cube Satellite, EIRSAT-1: Steady Analysis. In Proceedings of the 2018 AIAA SPACE and Astronautics Forum and Exposition, Orlando, FL, USA, 17–19 September 2018; AIAA 2018-5285. https://doi.org/10.2514/6.2018-5285.
69. Exolaunch GmbH. EXOpod CubeSat Deployer. Available online: https://exolaunch.com/exopod#1 (accessed on 26 August 2026).
70. SpaceX. Transporter-16 Mission. March 2026. Available online: https://www.spacex.com/launches/transporter16 (accessed on 26 August 2026).

Disclaimer/Publisher's Note: The statements, opinions and data contained in all publications are solely those of the individual author(s) and contributor(s) and not of MDPI and/or the editor(s). MDPI and/or the editor(s) disclaim responsibility for any injury to people or property resulting from any ideas, methods, instructions or products referred to in the content.